



A digital-twin solution for floating offshore wind turbines validated using a full-scale prototype

Emmanuel Branlard¹, Jason Jonkman¹, Cameron Brown², and Jiatian Zang²

¹National Renewable Energy Laboratory, Golden, CO 80401, USA

²Stiesdal Offshore A/S, Denmark

Correspondence: E. Branlard (emmanuel.branlard@nrel.gov)

1 **Abstract.** In this work, we implement, verify, and validate a physics-based digital twin solution applied to a floating offshore
2 wind turbine. The digital twin is validated using measurement data from the full-scale TetraSpar prototype. We focus on the
3 estimation of the aerodynamic loads, wind speed, and section loads along the tower, with the aim at estimating the fatigue
4 life-time of the tower. Our digital twin solution integrates: 1) a Kalman filter to estimate the structural states based on a linear
5 model of the structure and measurements from the turbine, 2) an aerodynamic estimator, and 3) a physics-based virtual sensing
6 procedure to obtain the loads along the tower. The digital twin relies on a set of measurements that are expected to be available
7 on any existing wind turbine (power, pitch, rotor speed, and tower acceleration), and motion sensors that are likely to be
8 standard measurements for a floating platform (inclinometers and GPS sensors). We explore two different pathways to obtain
9 physics-based models: a suite of dedicated Python tools implemented as part of this work, or the OpenFAST linearization
10 feature. In our final version of the digital twin, we use components from both approaches. We perform different numerical
11 experiments to verify the individual models of the digital twin. In this simulation realm, we obtain estimated damage equivalent
12 loads with an accuracy of the order of 5% to 10%. When comparing the digital twin estimations with the measurements from
13 the TetraSpar prototype, the errors increased to 10%-15% on average. Overall, the accuracy of the results appears promising
14 and demonstrates the possibility to use digital twin solutions to estimate fatigue loads on floating offshore wind turbines. A
15 natural continuation of this work would be to implement the monitoring and diagnostics aspect of the digital twin, to inform
16 operation and maintenance decisions. The digital twin solution is provided with examples as part of an open-source repository.

17 1 Introduction

18 The offshore floating wind turbine market is expected to grow in the next decades as the technology is gaining in maturity,
19 with several floating wind turbine prototypes already tested and commissioned, such as the TetraSpar, developed by Sties-
20 dal Offshore(Stiesdal Offshore, 2022). Operation & maintenance (O&M) costs can account for approximately one-third of
21 offshore wind farm life-cycle expenditures for a fixed-bottom project and are expected to be higher for remote (floating)
22 projects (Castella, 2020). Reducing the O&M costs is therefore an impactful and effective means to lower the costs of floating
23 offshore projects. Digital twin solutions are increasingly being considered to follow products during their life cycle to assess
24 component conditions, guide predictive maintenance, and thereby reduce O&M costs. A review of digital twins for power sys-



25 tems is found in Song et al. (2023). Digital twins often include a virtual sensing component, whose role consists in providing
26 information that are not measured by the physical system, and a structural health monitoring component to assess the condition
27 of the system. Virtual sensing technology is usually achieved using physics-based or data-driven approaches; both approaches
28 relying on measurements from the physical system to infer and extrapolate information about its current state. Physics-based
29 approaches use a numerical model of the system, whereas data-driven approaches either use ad-hoc algorithms or machine-
30 learning techniques. This work presents the development, verification and validation of a physics-based digital twin for floating
31 wind turbines, as a proof of concept for future maturation of the technology.

32 Digital twins for wind turbine applications have recently become a topic of research interest. The current authors explored
33 the topic of physics-based digital twins in previous work, where a method to estimate tower loads on land-based turbines was
34 developed (Branlard et al., 2020a, b). The approach relied on a Kalman filter model (Kalman, 1960; Zarchan and Musoff,
35 2015), which combines a linear physics-based model of the structure with measurements from the turbine to perform a virtual
36 sensing of the tower section loads and estimate the fatigue of this component. The measurement data was taken from the
37 supervisory control and data acquisition (SCADA) system using sensors readily available on most turbines. The approach used
38 a mix between an augmented Kalman filter approach (Lourens et al., 2012), where the loads are estimated with the states of the
39 system, and a physics-based aerodynamic estimator for aerodynamic thrust. Bilbao et al. (2022) used a Gaussian process latent
40 force model instead to estimate the forcing of the system, and thereby obtain the section loads along the tower. Drivetrains are
41 another component that has recently been an application of digital twin, with physics-based approaches presented for instance
42 in (Mehlan et al., 2022, 2023), and data-driven models in Kamel et al. (2023).

43 In spite of the term “digital twin” becoming recently popular, it is heavily based on the fields of structural-health monitoring
44 and load estimations (or more generally, virtual sensing), which have long been topics of research. For instance, Iliopoulos
45 et al. (2016) used physics-based modal decomposition to estimate the dynamic response on the substructure of a fixed-bottom
46 wind turbine. Neural networks have been used to establish transfer functions or surrogate models based on SCADA data to
47 obtain wind turbine loads with the aim of performing conditional monitoring (see, e.g. Cosack (2010); Schröder et al. (2018)).
48 Kalman filters were introduced in fields other than wind energy to perform load estimation, for instance in the following
49 references: Auger et al. (2013); Ma and Ho (2004); Eftekhar Azam et al. (2015); Lourens et al. (2012). Kalman filtering
50 has been extensively used in wind energy to estimate rotor loads and improve wind turbine control, see, e.g. Boukhezzar
51 and Siguerdidjane (2011); Selvam et al. (2009); Bottasso and Croce (2009); Bossanyi (2003). Load estimations were also
52 achieved using hybrid-techniques combining physics based on SCADA data by Noppe et al. (2016). Other load estimation
53 techniques may be used, such as lookup tables (Mendez Reyes et al., 2019), modal expansion (Iliopoulos et al., 2016), machine
54 learning (Evans et al., 2018), neural networks (Schröder et al., 2018), polynomial chaos expansion (Dimitrov et al., 2018),
55 deconvolution (Jacquelin et al., 2003), or load extrapolation (Ziegler et al., 2017).

56 In this work, we build on our previous work and present a digital twin solution for floating wind turbines that relies on
57 physics-based models and a Kalman filter. We apply the digital twin to the TetraSpar structure and use measurements from
58 the full-scale prototype. In section 2, we provide an overview of our digital concept, the vision for future application, and the
59 TetraSpar prototype on which the digital twin is applied. In section 3, we present the individual components of the digital twin,



60 and run some isolated verification studies on them. In section 4, we present results from the digital twin application first using
 61 numerical experiments, and then using measurements from the TetraSpar prototype, before concluding. To avoid lengthening
 62 the main text, we provide derivations (some being important contributions of this work) and additional results in appendices.

63 2 Overview of the digital twin concept

64 In this section, we provide an overview of our digital twin concept and how it is applied in this study.

65 2.1 Long-term vision of the digital twin concept

66 Many definitions and applications of digital twins are possible. The vision for the concept discussed in the work is to follow
 67 the life-cycle of a wind turbine in real-time and ultimately provide tangible signals to inform O&M decisions. Our goal is to
 68 achieve this by relying only on measurements expected to be available on most wind turbines, thereby avoiding the extra cost
 of adding sensors. We illustrate our approach and vision in Figure 1. The digital twin is intended to run in real-time on a cloud

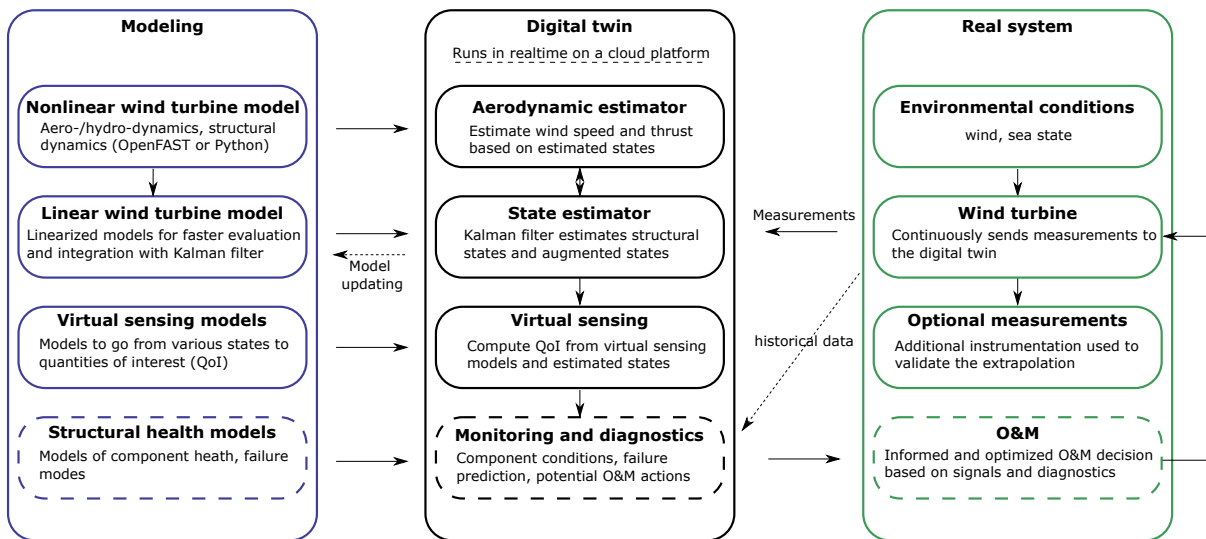


Figure 1. Overview of the digital twin concept. Dashes lines indicate features that are outside the current scope.

69
 70 platform. It combines a set of models (on the left of the figure) with data from the real system (on the right) to perform the
 71 estimation of various states and eventually produce diagnostics that can be use to inform the O&M. The data from the real
 72 system are taken from high-frequency measurements from the SCADA system (e.g., power, pitch, rotor speed, etc.). The states
 73 estimated by the digital twin include aerodynamic states (wind speed, thrust) and motions of the structure (e.g., surge, pitch,
 74 tower deflection). The core algorithm in the estimation is a Kalman filter that uses a linear wind turbine model. The estimated
 75 states are used in an “virtual sensing” step, to produce quantities of interests (QoI), such as the loads at key locations of the



76 structure. The QoI are then intended to be postprocessed by a monitoring and diagnostic tool to generate the data needed to
77 perform condition-based O&M.

78 **2.2 Narrowed scope**

79 The boxes in Figure 1 that are surrounded with dashes are not addressed in the current work, namely: the structural health
80 modeling, monitoring and diagnostics, and O&M decisions. These are essential steps necessary to achieve our final vision,
81 but they are postponed to future work. Dashed lines indicate possible options that may be exploited in the future but are also
82 outside of our scope: the use of historical data to assist in the diagnostics, the use of estimates to perform modeling updating,
83 and real time implementation.

84 This work therefore focuses on the estimation of states and environmental conditions under the assumption that the estimated
85 quantities can replace costly measurements and eventually be used for O&M decisions. We intend to provide a proof of concept
86 paving the way for future commercial applications. A detailed description of each of the boxes surrounded with plain lines will
87 be provided in section 3.

88 **2.3 System studied**

89 **2.3.1 The TetraSpar prototype**

90 Throughout this article, the system studied is the TetraSpar floating offshore prototype. The system consists of a floating
91 platform and station keeping system developed by Stiesdal Offshore in collaboration with partners Shell, RWE and TEPCO
92 Renewable Power, and a 3.6-MW wind turbine with a rotor diameter of 130 m developed by Siemens Gamesa Renewable
93 Energy. A sketch of the system is provided in Figure 2. The prototype was installed off the coast of Norway and commissioned
94 in November 2021. The prototype turbine is equipped with additional sensors (labeled “Optional measurements” in Figure 1),
95 which we will use to validate the estimated QoI.

96 **2.3.2 Numerical experiments**

97 Prior to using measurement data, we will use simulations (referred to as “numerical experiments”) in place of the real system
98 to feed-in data to the digital twin. The advantage of this approach is that the QoI are directly accessible and can be compared
99 to the estimates for verification purposes.

100 Data for the numerical experiments is obtained using OpenFAST simulations (Jonkman et al., 2023). A model of the
101 TetraSpar floating platform and the wind turbine was implemented in OpenFAST based on data provided by the manufac-
102 turers. The operating conditions of the turbine were extracted from SCADA data and a controller was tuned to approximate
103 these conditions. We use the following modules of OpenFAST (see Table 2, and Jonkman et al. (2023)): MAP (mooring lines),
104 HydroDyn (hydrodynamics), ElastoDyn (tower and blade elasticity; rigid floater), AeroDyn (aerodynamics), InflowWind (wind
105 inflow), ServoDyn (controller interface).

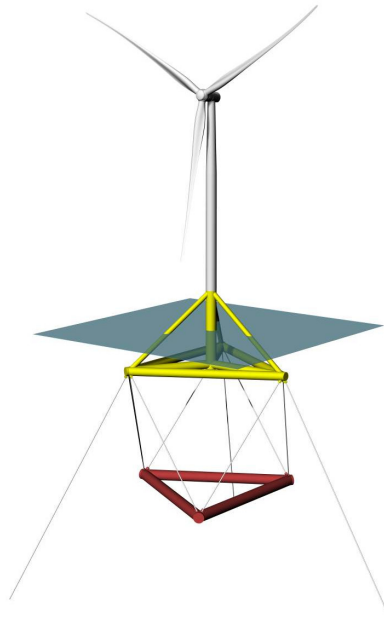


Figure 2. Sketch of the TetraSpar prototype

106 For the numerical experiments, we use synthetic turbulent wind fields generated using TurbSim (Jonkman and Buhl (2006)).
107 In particular, we will often use the same wind field, that we will refer to as the “turbulent step”, where a deterministic ramp
108 and drop are added to a turbulent field. The advantage of this 10-min wind field is that it covers all the operating regions of the
109 turbine in a **challenging way**. The wind speed at hub height for the turbulent step can be seen in Figure 6.

110 2.3.3 Main aspects of the structural model

111 We model the structure using a set of 8 degrees of freedom (DOFs), as illustrated in Figure 3. The platform is represented as a
112 rigid body and its motion is described using 6 DOFs: surge, sway, heave, roll, pitch, yaw, respectively noted $x, y, z, \phi_x, \phi_y, \phi_z$.
113 The tower bending in the fore-aft direction is represented using one generalized DOF, q_t , associated with a Rayleigh-Ritz shape
114 function, taken as the first fore-aft mode shape of the tower (see, e.g., Branlard (2019)). The shape function along the tower
115 height, z_t , is written $\Phi(z_t)$, with $\Phi(0) = 0$ at the tower bottom, and $\Phi(L_T) = 1$ at the tower top, where L_T is the tower length.
116 The shaft rotation is noted ψ , so that the rotation speed of the rotor is $\dot{\psi}$ where the dotted notation indicates differentiation
117 with respect to time. The rotor-nacelle-assembly (RNA) is modeled as a rigid body. The full vector of DOFs is therefore:
118 $\mathbf{q} = [x, y, z, \phi_x, \phi_y, \phi_z, q_t, \psi]$. The equations of motion will be recast into a first order form by concatenating the vector of
119 DOFs and its time derivative: $\mathbf{x} = [\mathbf{q}, \dot{\mathbf{q}}]$.

120 In this work, we ~~perform a simplifying assumptions, e.g., neglecting~~ the influence of nacelle yaw on the system. The mea-
121 surement data is conveniently provided in the fore-aft and side-side system of the nacelle. The main assumption is therefore

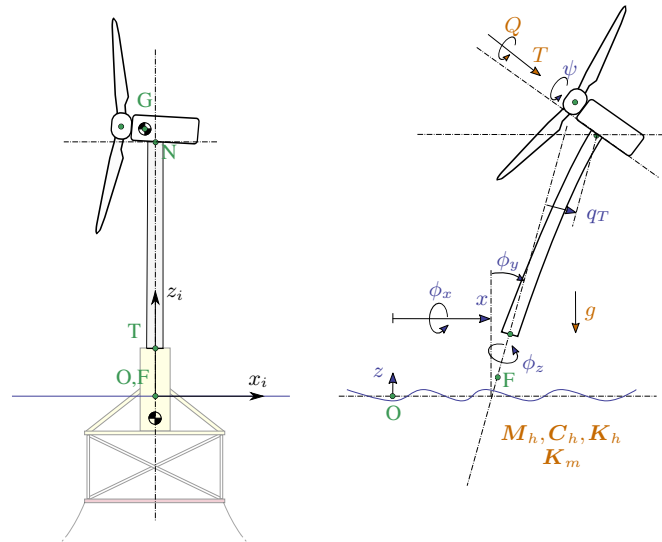



Figure 3. Notations for the structural modeling of the floating wind turbine, assuming no yawing of the nacelle. Left: main points (F, T, N, O, G) and inertial coordinate system (i). Right: degrees of freedom ($x, y, z, \phi_x, \phi_y, \phi_z, q_t, \psi$) and main loads: aerodynamics (T, Q), hydrodynamics (6×6 mass, damping and stiffness matrices: M_h, C_h, K_h . Wave excitation force neglected), mooring (6×6 stiffness matrix K_m) and gravity (g).

122 that we assume a rotational symmetry of the platform and mooring system about the yaw axis. We intend to lift this assumption
 123 in future work 

124 3 Individual components of the digital twin

125 In this section, we describe and verify the individual components of the digital twin presented in Figure 1. In section 4, we will
 126 present applications of the digital twin where all the individual components are combined together.

127 3.1 Wind turbine measurements

128 The measurements used as inputs to the digital twin are listed in Table 1. These outputs are stored in a database at a sampling
 129 rate of 25 Hz. We expect these measurements to be standard sensors for any floating wind turbine. The TetraSpar prototype is
 130 equipped with additional measurements that will be used to validate the implementation of the digital twin (see section 4).

131 3.2 Nonlinear wind turbine models

132 Similar to our previous work (Branlard et al., 2020b), we use two different pathways to obtain nonlinear and linear models of
 133 floating wind turbines: OpenFAST and WELIB (Wind Energy LIBrary, Branlard (2022)). The different modeling approaches
 134 are illustrated in Table 2 and further presented below.



Table 1. Measurements used as inputs to the digital twin.

Signal	Symbol
Blade pitch angle	θ_p
Rotor speed	$\dot{\psi}$
Generator torque*	Q_g
Surge and Sway	x, y
Roll and Pitch	ϕ_x, ϕ_y
Nacelle accelerations	$\ddot{\mathbf{r}}_N$

* Obtained from the power measurement using Equation 2.

Table 2. Approaches and tools used to obtain nonlinear and linear models.

Approach	Tool	Usage	Formulation & Linearization
1 OpenFAST	OpenFAST (ElastoDyn, HydroDyn, MAP, AeroDyn)	Structural model Hydrodynamics Mooring Aerodynamics Virtual sensing	Numerical and analytical
2 WELIB (Python tools)	YAMS	Structural model Virtual sensing	Analytical
	pHydroDyn	Hydrodynamics	Numerical
	pyMAP	Mooring	Numerical

135 The OpenFAST approach was described in Section 2.3.2. The WELIB approach consists of a set of dedicated open-source
 136 Python tools. We developed this Python code to offer additional modularity and granularity, for instance to allow for: simple
 137 linearization of the hydrodynamics (obtention of 6x6 matrices), linearization of hydrodynamics with respect to wave elevation,
 138 linearization with respect to parameters (Jonkman et al., 2022), and interactive time-stepping of linear and nonlinear models.
 139 One shortcoming is that WELIB does not cover the full range of options available with OpenFAST, which is a continuously
 140 evolving, extensively verified and validated tool. For this work, we implemented the following tools in WELIB: 1) YAMS, a
 141 symbolic structural dynamics package to obtain the equations of motion of an assembly of rigid and flexible bodies analytically,
 142 and allow for their analytical linearization (Branlard and Geisler, 2022); 2) pHydroDyn, a Python version of the module
 143 HydroDyn (with a subset of HydroDyn’s functionality) to determine the hydrodynamic loads; and 3) pyMAP, a wrapper around
 144 the MAP module of OpenFAST, to obtain the mooring quasi-statics. With these three additions, it is possible to perform
 145 nonlinear simulations of floating wind turbines using WELIB and perform comparisons with OpenFAST. The benefits of
 146 WELIB over OpenFAST is the possibility to obtain analytical linear models and gain physical intuitiveness on the model.
 147 Results will be presented in see Section 3.3.



148 3.3 Linear wind turbine models

149 As part of our digital twin concept, we have chosen to use linear wind turbine models and a Kalman filter for the core of the
150 state estimation (see Section 3.5). Nonlinear models and an extended Kalman filter could be considered in future iterations. In
151 this section, we describe how the linear models from OpenFAST and WELIB are obtained.

152 3.3.1 OpenFAST linearization

153 OpenFAST can provide full-system linearization of its underlying nonlinear models by using a mix of analytically- and finite-
154 difference-derived Jacobians (Jonkman and Jonkman, 2016; Jonkman et al., 2018). The linearization process provides the
155 state-space model ($\delta\dot{\mathbf{x}} = \mathbf{A}\delta\mathbf{x} + \mathbf{B}\delta\mathbf{u}$) and output equation ($\delta\mathbf{y} = \mathbf{C}\delta\mathbf{x} + \mathbf{D}\delta\mathbf{u}$) for small perturbations (indicated with δ) of
156 the internal states (\mathbf{x}), inputs (\mathbf{u}) and outputs (\mathbf{y}) of OpenFAST, around the linearized operating point. OpenFAST provides the
157 linear model for the entire set of states, inputs and outputs present in the model (including virtual sensor-type outputs typically
158 written to an output file and not used internally). In this work, we extract subsets of the \mathbf{A} , \mathbf{B} , \mathbf{C} , \mathbf{D} matrices and combine
159 them to form the linear model of the state estimator (see Section 3.5).

160 3.3.2 WELIB linearization

161 WELIB performs the linearization of the structure, hydrodynamics and moorings independently, before combining them into
162 one model. The aerodynamic loads are not linearized because a dedicated aerodynamic estimator is used in this work (see
163 Section 3.4). The steps are as follows:

- 164 – The structural equations are linearized analytically using our symbolic framework (Branlard and Geisler, 2022). We
165 introduce a notion of “augmented inputs” to linearize the equations of motion without an explicit knowledge of the
166 external forces. The process is described in Appendix A.
- 167 – We compute the 6×6 linearized rigid-body hydrodynamics matrices (mass matrix \mathbf{M}_h , damping matrix \mathbf{C}_h and stiffness
168 matrix \mathbf{K}_h) corresponding to the six rigid-body motions of the platform. We obtain them using numerical differentiation
169 in two different ways: 1) using the Python implementation of the HydroDyn module by performing rigid-body perturba-
170 tion of the full platform, or, 2) using full-system linearization of the HydroDyn module. The latter provides Jacobians of
171 the hydrodynamic loads as function of motions of the individual hydrodynamic analysis nodes (of which models often
172 have hundreds to thousands of). To transfer these individual Jacobians to the reference point and obtain the 6×6 ma-
173 trices, we developed and used the method presented in Appendix B. The consistency between the two approaches was
174 verified. The second approach is not straightforward to implement, therefore, we upgraded the OpenFAST HydroDyn
175 driver to provide the 6×6 hydrodynamic matrices directly without the need to use the full-system linearization.
- 176 – The linearized 6×6 mooring stiffness matrix, \mathbf{K}_m , is obtained by calling the linearization feature of the MAP module,
177 and transferring the Jacobian to the reference point using the method outlined in Appendix B.
- 178 – The linearized equations of motion are assembled as:



179 $[M_0 + Q_0 M_h] \delta \ddot{\mathbf{q}} + [C_0 + Q_0 C_h] \delta \dot{\mathbf{q}} + [K_0 + Q_0 (K_h + K_m)] \delta \mathbf{q} = \delta \mathbf{f}_a + \delta \mathbf{f}_h$ (1)

180 where the matrices with subscript 0 originate from the linearization of the structure (see Appendix A). The term Q_0 is used here
 181 to map the 6 rigid-body platform degrees of freedom to the full vector of degrees of freedom. The term $\delta \mathbf{f}_a$ is an approximation
 182 of the aerodynamic loads, and will be discussed in Section 3.4. The term $\delta \mathbf{f}_h$ is an approximation of the hydrodynamic wave-
 183 excitation loads and it will be mapped into the inherent model noise of the Kalman filter in Section 3.5. Equation 1 is recast
 184 into a first order system to obtain the state matrix A .

185 **3.3.3 Verification of the linear models**

186 In this section, we compare results from the OpenFAST nonlinear model, the OpenFAST linear model and the WELIB linear
 187 model, for free-decay simulations of the TetraSpar structure. The OpenFAST linear model is obtained about the operating
 188 point defined by $\mathbf{q}_0 = \mathbf{0}$ and $\dot{\psi}_0 = 10$ rpm. All models (including the OpenFAST nonlinear model) use 8 DOFs. The initial
 189 conditions are set to $\mathbf{q} = [1, -1, 0.6, 0.5, 0.5, 0, -0.2, 0]$ (in m and deg) and $\dot{\psi} = 10$ rpm, after which the structure is free to
 190 decay.

191 The time responses from the linear and nonlinear models are in strong agreement when only the structure is considered
 192 (see results in Appendix C). Below, we present results for a model that includes hydrodynamics, but without wind or external
 waves (still water). We set the hydrodynamic drag to zero due to the difficulty in linearizing this term and will let the state

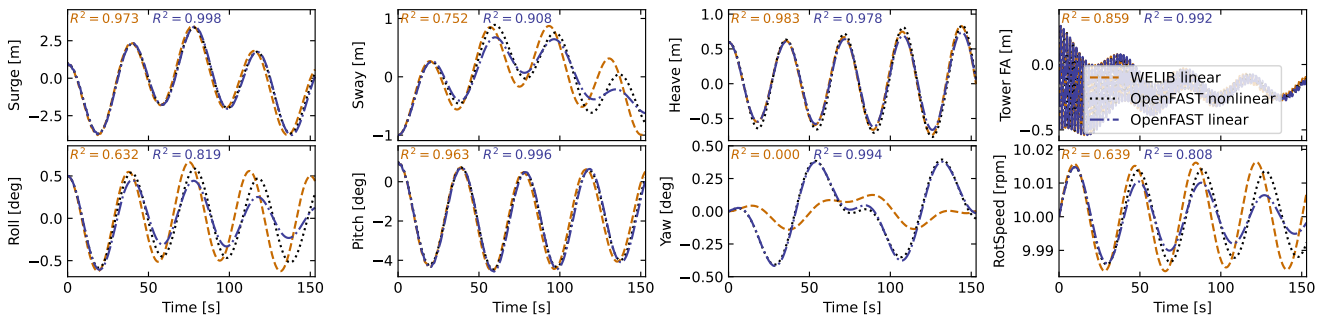


Figure 4. Free decay of the structure using non linear and linear models for a case including moorings and hydrodynamics (still water). Time series of the main DOFs.

193
 194 estimator account for this modeling uncertainty. Results of the free-decay simulation are given in Figure 4, for a time period
 195 of 153 s corresponding to the surge frequency. When hydrodynamics is included, the time responses from the linear models
 196 are in strong agreement with the nonlinear OpenFAST results for the surge, heave, pitch and tower fore-aft DOFs. The sway,
 197 roll, and rotor speed responses tend to drift as the simulation time advances. The WELIB linear model has difficulty capturing
 198 the yaw response. We believe that some of the error in the yaw signal is due to differences between the formulations of the
 199 three-dimensional rotations in OpenFAST and WELIB, resulting in a difference of coupling between the DOFs. The coefficient
 200 of determination (R^2) is indicated in Figure 4, comparing the linear models to the reference OpenFAST simulations for each
 201 response. In all cases, the OpenFAST linear model is closer to the nonlinear OpenFAST model than the WELIB model.



202 To further quantify the differences between the models, we compare the natural frequencies obtained using the OpenFAST
 linear and WELIB linear models in Table 3. Overall, the frequencies between the two linear formulations agree very well (less

Table 3. Comparison of system frequencies obtained using the WELIB and OpenFAST linear models with and without hydrodynamics (no added mass, damping, hydrostatics, or wave excitation)

Mode	Structure + mooring			Structure + mooring + hydrodynamics		
	OpenFAST [Hz]	WELIB [Hz]	Rel. Err [%]	OpenFAST [Hz]	WELIB [Hz]	Rel. Err [%]
Surge	0.0088	0.0088	-0.2	0.0067	0.0065	-2.4
Sway	0.0088	0.0088	-0.1	0.0067	0.0068	0.7
Yaw	0.0163	0.0162	-1.0	0.0128	0.0128	-0.3
Pitch	0.0879	0.0886	0.7	0.0253	0.0257	1.6
Roll	0.0894	0.0902	0.9	0.0256	0.0266	4.0
Heave	NA	NA	NA	0.0276	0.0276	-0.2
Tower FA	0.5782	0.5789	0.1	0.5129	0.5145	0.3

203
 204 that 2.5% relative error), except for the roll frequencies (4% error) with hydrodynamics. Given the results of this section, we
 205 will continue this study using the OpenFAST linear model. We expect that continuous development of WELIB will further
 206 narrow the gap with OpenFAST in the future.

207 3.4 Aerodynamic estimator

208 In Section 3.3, we indicated that the linear models were derived without accounting for aerodynamics. Instead, we choose to
 209 include the aerodynamic contribution separately within the digital twin. The reason for this choice is that the determination of
 210 the aerodynamic loads is essential to capturing the main loading and deflections of the structure, in particular the tower, and,
 211 the aerodynamic loads vary significantly over the range of operating conditions. Therefore, separating this contribution limits
 212 the need to obtain different linearized models for different operating conditions. We have successfully applied this approach
 213 in the past (Branlard et al., 2020a). In this work, we extend this approach to accommodate the floating wind application. The
 214 different elements of the aerodynamic estimator consist of: a torque estimator, aerodynamic maps, and a wind speed estimator.

215 3.4.1 Kalman filter for torque estimation

216 We assume that the power and rotor speed are reliable measurement signals, and we further assume that the generator torque
 217 (relative to the low-speed shaft) can be inferred from the power signal as:

$$218 \quad Q_g = \frac{P}{\dot{\psi}} \frac{1}{n\eta_{DT}(\dot{\psi})} \quad (2)$$



219 where η_{DT} is the drivetrain (gearbox and generator) efficiency, and n is the gear ratio. For the TetraSpar, $n = 1$, and we assume
 220 $\eta_{DT} = 1$. The dynamics equation of the drivetrain is modeled as:

$$221 \quad J_{DT}\ddot{\psi} = Q - Q_g \quad (3)$$

222 where J_{DT} is the inertia of the drivetrain about the shaft axis. If we assume that the generator torque is a measurement, then an
 223 augmented Kalman filter (Lourens et al., 2012) can be used to estimate the aerodynamic torque Q , using the following state
 224 equation:

$$225 \quad \begin{bmatrix} \dot{\psi} \\ \ddot{\psi} \\ \dot{Q} \end{bmatrix} = \begin{bmatrix} 0 & 1 & 0 \\ 0 & 0 & \frac{1}{J_{DT}} \\ 0 & 0 & 0 \end{bmatrix} \begin{bmatrix} \psi \\ \dot{\psi} \\ Q \end{bmatrix} + \begin{bmatrix} 0 \\ -\frac{1}{J_{DT}} \\ 0 \end{bmatrix} Q_g \quad (4)$$

226 A random walk approach is used for the evolution of the torque, that is, $\dot{Q} = 0$ and the Kalman filter adds further model noise
 227 to this equation. The measurement equation of the Kalman filter is:

$$228 \quad \begin{bmatrix} \dot{\psi} \\ Q_g \end{bmatrix} = \begin{bmatrix} 0 & 1 & 0 \\ 0 & 0 & 0 \end{bmatrix} \begin{bmatrix} \psi \\ \dot{\psi} \\ Q \end{bmatrix} + \begin{bmatrix} 0 \\ 1 \end{bmatrix} Q_g \quad (5)$$

229 In the following, we will write \hat{Q} , the aerodynamic torque obtained using the method outlined above. We will present verifica-
 230 tion results in Section 3.4.4.

231 3.4.2 Aerodynamic maps

232 It is commonly accepted that the aerodynamic performances of a wind turbine mostly depends on the tip-speed ratio and the
 233 pitch angle of the blade. With compliant structures, the bending of the blade, the bending of the tower, and the motions of the
 234 floating platform (in particular the platform pitch) will also affect the aerodynamic performances. These motions are to a large
 235 extent a function of the mean wind speed. Therefore, we suggest to tabulate the aerodynamic performances as function of wind
 236 speed (U), rotor speed ($\dot{\psi}$), blade pitch (θ_p), and platform pitch ϕ_y (assumed to be in the fore-aft direction). The power and
 237 thrust coefficients, respectively noted C_P and C_T , are precomputed using aeroelastic simulations in OpenFAST for a discrete
 238 set of values of the 4 input parameters. In the simulations, the blade and tower elasticity are accounted for. To limit the number
 239 of simulations, only the points that are within reasonable proximity of the regular operating conditions of the wind turbine are
 240 computed. The 4D aerodynamic maps are precomputed as follows:

$$241 \quad C_P(U, \dot{\psi}, \theta_p, \phi_y), \quad C_T(U, \dot{\psi}, \theta_p, \phi_y) \quad (6)$$

$$242 \quad U \in \{2, 3, \dots, 25\} \text{ m.s}^{-1}, \quad \dot{\psi} \in \{5, 5.5, \dots, 18\} \text{ rpm}, \quad (7)$$

$$243 \quad \theta_p \in \{-1, 0, \dots, 30\} \text{ deg}, \quad \phi_y \in \{-10, 0, 15\} \text{ deg} \quad (8)$$

244 The precomputed values are stored in a database.



245 **3.4.3 Wind speed estimation**

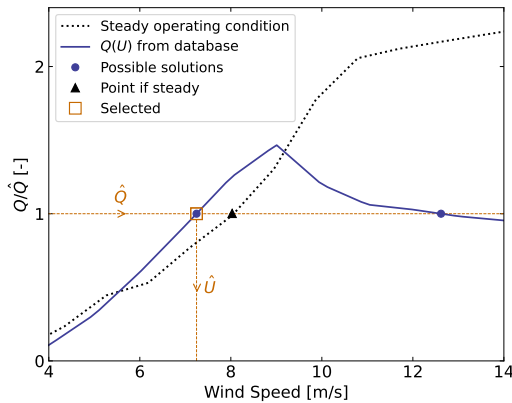
246 The digital twin uses the aerodynamic map database to estimate the wind speed and aerodynamic thrust. For a given air density
 247 (ρ), rotor radius (R), and given measurements $\tilde{\psi}, \tilde{\theta}_p, \tilde{\phi}_y$, the aerodynamic torque and thrust are readily obtained as function of
 248 wind speed from the database:

249
$$Q(U) = \frac{1}{2} \rho \frac{U^3}{\tilde{\psi}} \pi R^2 C_P(U, \tilde{\psi}, \tilde{\theta}_p, \tilde{\phi}_y), \quad T(U) = \frac{1}{2} \rho U^2 \pi R^2 C_T(U, \tilde{\psi}, \tilde{\theta}_p, \tilde{\phi}_y) \quad (9)$$

250 where S.I. units are assumed for all variables. For a given estimated torque (\hat{Q}), the estimated wind speed (\hat{U}) is found such
 251 that:

252
$$Q(\hat{U}) - \hat{Q} = 0 \quad (10)$$

253 As illustrated in Figure 5, multiple values of \hat{U} can potentially satisfy Equation 10 because the aerodynamic torque is a
 nonlinear function of the wind speed. In such case, we use the steady state operating condition curve of the turbine to chose



254 **Figure 5.** Illustration of wind speed estimation in the case where multiple wind speed values match the target torque value \hat{Q}

255 between the multiple solutions (typically two), by selecting the point that is closest to this curve (see Figure 5). A relaxation
 256 scheme is also used, based on the previous estimate, to alleviate sudden jumps of the estimated wind speed.

257 **3.4.4 Verification of the aerodynamic estimator**

258 To verify the aerodynamic estimator, we ran an OpenFAST simulation of the TetraSpar with the “turbulent step” wind field
 259 mentioned in Section 2.3.2 and irregular waves computed with a significant wave height of $H_s = 6$ m and a peak spectral
 260 period of $T_p = 14$, which represent a fairly extreme sea state for the site of the TetraSpar prototype. The simulated values of
 261 $\dot{\psi}, \theta_p, \phi_y, Q_g$ are used as direct input to the aerodynamic estimator. Comparisons of the estimates with the OpenFAST outputs
 262 are shown in Figure 6. The shaded area on the figure represent the area where the generator torque is zero (turbine spinning
 263 up), and therefore, the wind speed estimator is not expected to work in that region. The top of the plots indicate the ratio of

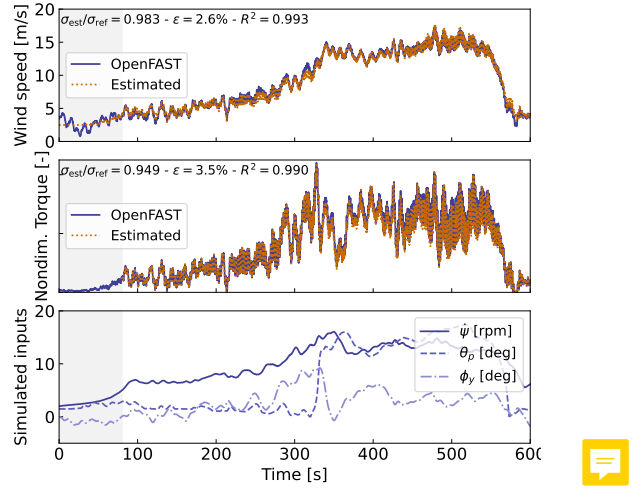


Figure 6. Example of aerodynamic estimation using “simulated measurements” from OpenFAST. Top: wind speed. Middle: Dimensionless torque. Bottom: structural inputs from the OpenFAST simulation provided to the estimator.

264 standard deviations, the mean relative error (ϵ) and the coefficient of determination (R^2). Throughout this article, we define the
 265 mean relative error of a quantity x as:

$$266 \quad \epsilon(x) = \text{mean}_i \left[\frac{|x_{\text{est}}[i] - x_{\text{ref}}[i]|}{\text{mean}(|x_{\text{ref}}|)} \right] \quad (11)$$

267 where x_{est} is the estimated signal, x_{ref} the reference signal, and $x[i]$ is the value of a signal at the time step i . Using the
 268 mean of $|x_{\text{ref}}|$ in the denominator avoids issue related to signals crossing 0. It results in lower mean relative error than if the
 269 instantaneous value was used, but the metric is still indicative of how far the two signals are on average.

270 To quantify the performance of the estimator, we reproduced the simulation above, but adding different noise levels to the
 271 measurements to account for measurement errors by the sensors. A Gaussian noise signal of zero mean and standard deviation
 272 $r\sigma$ is added to each input, where r is the noise level and σ is the standard deviation of the clean input. The results are shown in
 Table 4. As expected, the error in the estimation increases with increasing noise levels. This numerical experiment provides a

Table 4. Mean relative error (ϵ) of the wind speed, torque and thrust estimates, for increasing noise levels.

Noise level	0%	1%	5%	10%	20%
Wind Speed	2.6%	2.6%	3.1%	4.1%	6.7%
Torque	3.5%	3.8%	5.0%	6.8%	11.1%
Thrust	4.1%	5.1%	5.6%	7.3%	11.6%

273
 274 rough quantification of the errors that can be expected from the aerodynamic estimator.



275 3.5 State estimator

276 In this work, we follow a similar approach to our previous work (e.g. Branlard et al. (2020a)), where an augmented Kalman
 277 filter is used to estimate states and loads. The Kalman filter used in the aerodynamic estimator (Section 3.4) is augmented
 278 with additional states and outputs. The Kalman filter uses two linear models: a state-equation, describing the time evolution of
 279 the states, and an output equation, describing how the measurements are related to the states and inputs. The state and output
 280 equations are written:

$$281 \delta \dot{\mathbf{x}}_{KF} = \mathbf{X}_x \delta \mathbf{x}_{KF} + \mathbf{X}_u \delta \mathbf{u}_{KF} + \mathbf{w}_x \quad (12)$$

$$282 \delta \mathbf{y}_{KF} = \mathbf{Y}_x \delta \mathbf{x}_{KF} + \mathbf{Y}_u \delta \mathbf{u}_{KF} + \mathbf{w}_y \quad (13)$$

283 where $\delta \mathbf{x}_{KF}$, $\delta \mathbf{u}_{KF}$, and $\delta \mathbf{y}_{KF}$ are the state, input, and output¹, respectively, \mathbf{X}_x , \mathbf{X}_u , \mathbf{Y}_x , and \mathbf{Y}_u are the system matrices that
 284 relate the different system vectors, and, \mathbf{w}_x and \mathbf{w}_y are Gaussian processes represented modeling noise. The output vector,
 285 $\delta \mathbf{y}_{KF}$, is also referred to as the “measurement” vector, because it corresponds to the measured signals. At a given time step,
 286 the Kalman filter algorithm uses the system matrices, a set of measurements, and an a-priori knowledge of the model and
 287 measurement uncertainties to estimate the state vector (Kalman, 1960; Zarchan and Musoff, 2015).

288 In this work, we design the state estimator such that the state vector contains the structural degrees of freedom ($\delta \mathbf{q}$ and $\delta \dot{\mathbf{q}}$)
 289 and the aerodynamic torque (Q), and the input vector consists of the thrust (obtained with the aerodynamic estimator), and
 290 the generator torque (obtained from the power). These design choices were guided by our previous work on the topic. For
 291 this choice of state and input variables, we build linear models for the state and output equations. We use the linear models
 292 described in Section 3.3 (the \mathbf{A} , \mathbf{B} , \mathbf{C} , \mathbf{D} matrices), to populate the system matrices of the Kalman filter. We provide additional
 293 details on how the relevant Jacobians are extracted in Section 3.6.1. Given our choice of system vectors, the state equation is:

$$294 \begin{bmatrix} \delta \dot{\mathbf{q}} \\ \delta \ddot{\mathbf{q}} \\ \dot{Q} \end{bmatrix} = \begin{bmatrix} \mathbf{0} & \mathbf{I} & \mathbf{0} \\ \mathbf{A}_{12} & \mathbf{A}_{22} & \frac{\partial \ddot{\mathbf{q}}}{\partial Q} \\ \mathbf{0} & \mathbf{0} & \mathbf{0} \end{bmatrix} \begin{bmatrix} \delta \mathbf{q} \\ \delta \dot{\mathbf{q}} \\ Q \end{bmatrix} + \begin{bmatrix} \mathbf{0} & \mathbf{0} \\ \frac{\partial \ddot{\mathbf{q}}}{\partial Q_g} & \frac{\partial \ddot{\mathbf{q}}}{\partial T} \\ 0 & 0 \end{bmatrix} \begin{bmatrix} Q_g \\ T \end{bmatrix} + \mathbf{w}_x \quad (14)$$

295 where, \mathbf{A}_{12} and \mathbf{A}_{22} are the two lower blocks of the \mathbf{A} matrix, and \mathbf{I} is the identity matrix. The Jacobians with respect to the
 296 loads are extracted from the \mathbf{B} and \mathbf{D} matrices. A random walk approach is used for the evolution of the torque Q (that is, we
 297 set $\dot{Q} = 0$). The output equation, which effectively relates the measurements to the system states and inputs, is set as:

$$298 \begin{bmatrix} \delta \tilde{\mathbf{q}} \\ \dot{\psi} \\ \ddot{\mathbf{r}}_N \\ Q_g \end{bmatrix} = \begin{bmatrix} \frac{\partial \tilde{\mathbf{q}}}{\partial \mathbf{q}} & \frac{\partial \tilde{\mathbf{q}}}{\partial \dot{\mathbf{q}}} & \frac{\partial \tilde{\mathbf{q}}}{\partial Q} \\ \mathbf{0} & \tilde{\mathbf{I}} & 0 \\ \frac{\partial \ddot{\mathbf{r}}_N}{\partial \mathbf{q}} & \frac{\partial \ddot{\mathbf{r}}_N}{\partial \dot{\mathbf{q}}} & \frac{\partial \ddot{\mathbf{r}}_N}{\partial Q} \\ \mathbf{0} & \mathbf{0} & 0 \end{bmatrix} \begin{bmatrix} \delta \mathbf{q} \\ \delta \dot{\mathbf{q}} \\ Q \end{bmatrix} + \begin{bmatrix} \mathbf{0} & \mathbf{0} \\ 0 & 0 \\ \frac{\partial \ddot{\mathbf{r}}_N}{\partial Q_g} & \frac{\partial \ddot{\mathbf{r}}_N}{\partial T} \\ 1 & 0 \end{bmatrix} \begin{bmatrix} Q_g \\ T \end{bmatrix} + \mathbf{w}_y \quad (15)$$

299 where $\ddot{\mathbf{r}}_N$ is the vector of nacelle accelerations, and $\tilde{\mathbf{q}} = \{\delta x, \delta y, \delta \phi_x, \delta \phi_y\}$ is the measurements of surge, sway, roll and pitch
 300 as given in Table 1.

¹In general, the Kalman filter system vectors are different from the ones used for the linearization presented in Section 3.3, therefore the subscript KF (for Kalman Filter) is added to these vectors.



301 The state and output equations are used as part of a Kalman filter algorithm implemented in WELIB, which continuously
302 takes as input the measurements from the wind turbine (corresponding to the left hand side of Equation 15). The process
303 and covariance matrices used within the Kalman filter algorithm (determining the values of w_x and w_y) are populated based
304 on the estimated standard deviations of the different states and outputs. At each time step, the thrust is estimated using the
305 aerodynamic torque of the previous time step and used as input. The result of the Kalman filter consists of the estimated states
306 and outputs at each time step. Sample simulation results will be provided in section 4.

307 3.6 Virtual sensing

308 Once the states are estimated by the Kalman filter, the virtual sensing step is used to derive quantities of interest (see Figure 1).
309 In this work, we focus on the estimation of the sectional loads along the tower using a physics-based model. We investigate
310 two methods to obtain these loads.

311 3.6.1 OpenFAST linearization outputs

312 The first method consists in using the linearization outputs of OpenFAST, namely using a subset of the equation $\delta y = C\delta x +$
313 $D\delta u$ (see Section 3.3.1). In general, if a QoI is present in the output vector of OpenFAST, it can be retrieved as follows. If the
314 variable is located at the row index k in the vector y , then this variable can be obtained from the states and inputs as:

$$315 [y]_k = [\delta y]_k + [y_0]_k = [C]_k \delta x + [D]_k \delta u + [y_0]_k \quad (16)$$

316 where $[\cdot]_k$ indicates that the row k of the matrix or column vector is used. In our case, $[y]_k$ in Equation 16 would for instance
317 be the sectional fore-aft bending moment at the height z_j along the tower, noted $\mathcal{M}_y(z_j)$. The advantages of using this method
318 are multiple: 1) the method is directly applicable to any other outputs computed by OpenFAST, 2) the calculation procedure
319 is linear and therefore computationally efficient, 3) if strain measurements are available at given heights, the rows $[C]_k$ and
320 $[D]_k$ could be included in the output equation of the Kalman filter (Equation 15) to provide information about the model's
321 expectation of these measurements, 4) the underlying linear model is consistent with the nonlinear model of OpenFAST. The
322 downside of the method is its linearity, in the sense that it is only valid close to the operating point and could lack important
323 nonlinear effects. The values of $[C]_k$, $[D]_k$ and $[y_0]_k$ would potentially need to be reevaluated if the system operates away
324 from the linearized operating point. One possible solution would be to introduce gain-scheduling to modify the linear system
325 based on the estimated wind speed.

326 3.6.2 Non-linear calculation (WELIB)

327 An alternative method consists in computing the section loads based on first principles using the formulation presented in
328 Branlard (2019). The calculation requires a knowledge of the tower-top loads and the full kinematics of the tower and nacelle
329 (position, velocity and acceleration). At a given time step, the kinematics are computed based on q , \dot{q} and \ddot{q} . The tower-top
330 loads are estimated based on the aerodynamic loads and the inertial loads of the rotor-nacelle assembly. We describe the method
331 in more details in Appendix D. The advantages are that nonlinearities are accounted for and the model is valid irrespectively of



332 the operating condition. The downside is that this method does not provide any of the four advantages offered by the OpenFAST
333 linearization method.

334 3.6.3 Verification of the section loads calculation

335 To verify the calculation of the section loads, we use the same “turbulent step” wind field and irregular sea state that was used
336 in Section 3.4.4. We assume that the time series of q , \dot{q} and \ddot{q} are entirely known, extracted from the OpenFAST simulation.
337 These time series are provided to the two section loads algorithms: the WELIB nonlinear algorithm, and the OpenFAST linear
338 algorithm.

339 We run two sets of virtual sensing. In the “ideal” set, the loads at the tower top are extracted from OpenFAST results and
340 provided to the two virtual sensing algorithms. In this ideal case, the linearized operating points of the OpenFAST linear
341 model is set as the mean of each of the OpenFAST time series values. Results for the ideal case are provided in Figure 7.
The two algorithms are able to reproduce the section loads of OpenFAST with relatively high accuracy, which verifies our two

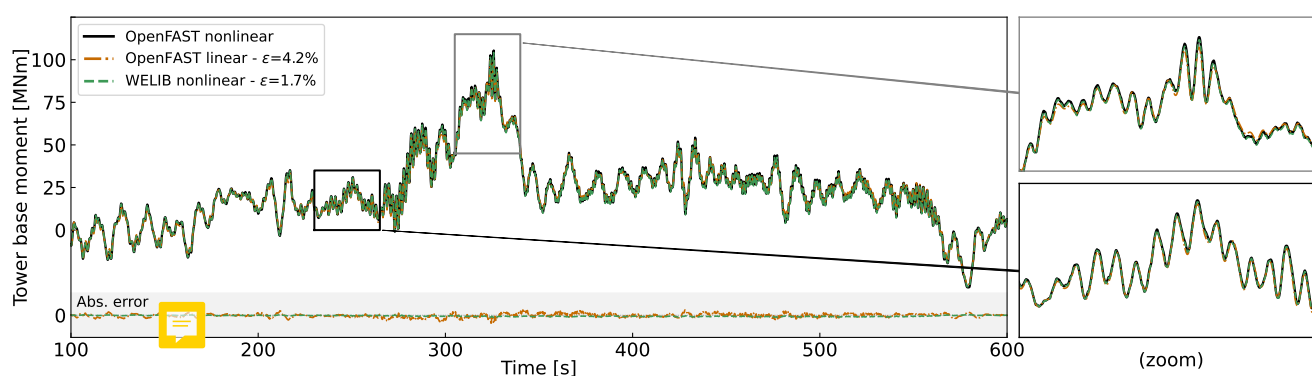


Figure 7. Tower fore-aft bending moment for the “turbulent step” and an irregular sea state as calculated by OpenFAST and compared to the WELIB nonlinear and OpenFAST linear method. The motion of the structure is determined by OpenFAST and provided to the two algorithms. The tower-top loads are also provided to the algorithms (“ideal” case, as opposed to Figure 8).

342
343 calculation procedures.

344 In the second set, labeled “unknown thrust”, the tower top loads are not provided to the algorithms, but instead, the aerody-
345 namic estimator mentioned in Section 3.4.4 is used to estimate the aerodynamic loads. This time, we do not set the linearized
346 operating point of the OpenFAST linear model to the mean value of the time series, but set it to the static equilibrium (without
347 loading). The results are provided in Figure 8. The accuracy of the section loads calculation is seen to deteriorate when the
348 aerodynamic loads are estimated with the aerodynamic estimator, which is expected. The damage equivalent load computed
349 with a Wöhler slope of $m = 5$ is found to be 3.7% lower with the OpenFAST linear method and 1.2% lower with the YAMS
350 nonlinear method compared to the value for reference signal.

351 The performances of both algorithms remain satisfactory because we observe that the extrapolated signals follow the refer-
352 ence OpenFAST nonlinear simulation. The relative error obtained with the OpenFAST linear algorithm is higher (13.3%) than

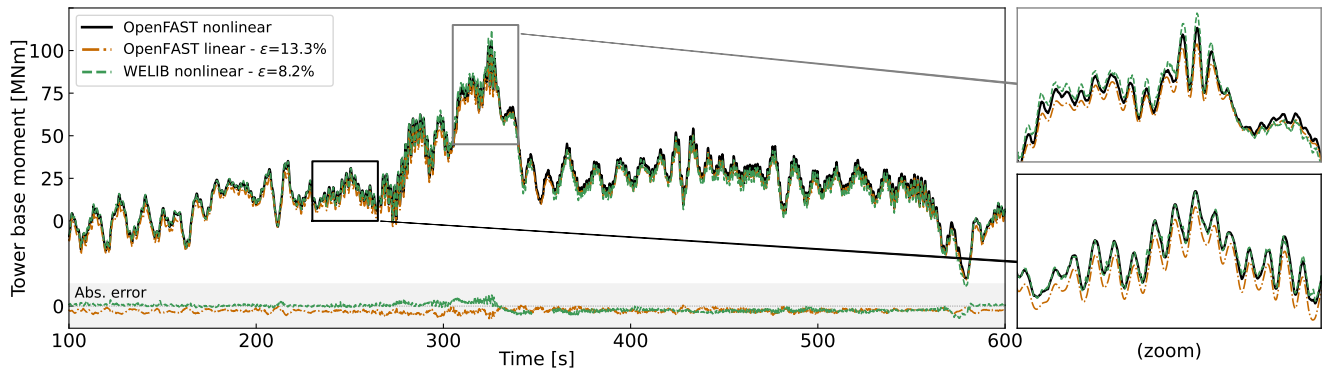


Figure 8. Tower fore-aft bending moment for the “turbulent step” and an irregular sea state as calculated by OpenFAST and compared to the WELIB nonlinear and the OpenFAST linear method. The motion of the structure is determined by OpenFAST and provided to the two other algorithms. The tower-top loads are estimated using the aerodynamic estimator (“unknown thrust” case, as opposed to the ideal case presented in Figure 7)

353 the one obtained using the WELIB nonlinear method (8.2%). The main source of error in the linear model is associated with
354 the fact that the linearization point was not tuned for this specific simulation. It is our simplifying design choice to use only
355 one linearization operating point throughout. Because of the loss of accuracy associated with this design choice, we will use
356 the WELIB nonlinear algorithm in the digital twin for the calculation of section loads.

357 We note that the variable that affects the most the fore-aft section loads is the platform pitch (ϕ_y), the tower fore-aft bending
358 degree of freedom (q_t), and then, the aerodynamic thrust. In this section, we assumed that all the states were known (including
359 ϕ_y and q_t), leading to great accuracy in the estimation of the section loads. The final verification step consists of providing
360 estimated states to the algorithm, which is the topic of the next section.

361 4 Applications of the digital twin

362 In section 3, the different components of the digital twin were introduced and tested using increasing level of complexity. In this
363 section, we combine the different components to form the digital twin. We begin using numerical experiments from OpenFAST
364 (see Section 2.3.2), similar to what was done in the previous section, before using measurements from the TetraSpar prototype.

365 4.1 Numerical experiment

366 First, we use the same “turbulent step” wind field and sea state that was used throughout section 3. The augmented states of the
367 system are determined at each time step using the state estimator described in Section 3.5. The measurements (see Table 1) are
368 taken from the nonlinear OpenFAST simulation. The wind speed and aerodynamic loads are estimated using the aerodynamic
369 estimator described in Section 3.4. The linear model is derived from linearized OpenFAST while the section loads in the tower
370 are obtained using the WELIB virtual sensing algorithm described in Section 3.6. The estimates from the digital twin are



compared with the reference nonlinear OpenFAST simulation results in Figure 9. A visual inspection of the time series reveals

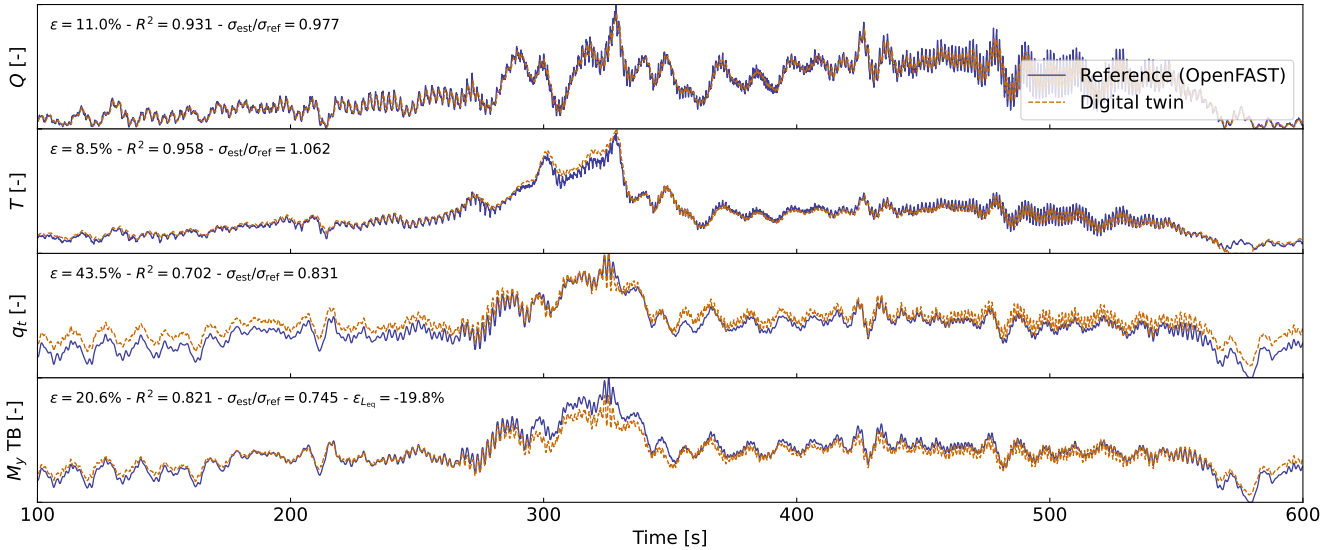


Figure 9. Estimated signals from the digital twin compared to results from an nonlinear OpenFAST simulation using the turbulent-step numerical experiment. From top to bottom: aerodynamic torque (Q), aerodynamic thrust (T), tower-top position (q_t), tower-bottom fore-aft bending moment (M_y , TB). Results are made dimensionless for confidentiality reasons.

371

372 that the digital twin is able to capture the main trends and fluctuations of the different signals. The match can be considered
 373 remarkable given that only the sensors provided in Table 1 are used by the digital twin. Metrics such as mean relative error (ϵ),
 374 and coefficient of determination (R^2) are indicated on the figure. Despite the visually appealing match, the metrics indicate
 375 that the tower-bottom moment has a mean error of $\epsilon = 21\%$. The damage equivalent load of the tower-bottom moment is
 376 underestimated by $\tilde{\epsilon}_{L_{eq}} = -21\%$, where we define:

$$377 \quad \tilde{\epsilon}(L_{eq}) = \frac{L_{eq,est} - L_{eq,ref}}{L_{eq,ref}} \quad (17)$$

378 Differences in damage equivalent loads typically indicate differences in the frequency content of the signals. We compare
 379 the frequency content of the estimated signals with the reference signals in Figure 10. The low-frequency content (below 1 Hz)
 380 is reasonably well captured, in line with the visual inspection of Figure 9. Unfortunately, no clear trend is found for the high
 381 frequency content: the power spectra of the aerodynamic loads indicate an underestimation whereas the spectra of the tower-top
 382 position and tower-bottom bending moment tend to have higher energy content. As shown in previous studies (Branlard et al.,
 383 2020a), **adequate filtering of the input measurements can be used to tune the energy content at high frequencies.**

384 To quantify the errors in the estimation under a wider set of operating conditions, we ran 10-min simulations for a set of
 385 wind speeds under normal turbulent conditions and sea states. We selected wind speeds from 5 to 20 m/s using 10 different
 386 seeds per bin of wind speed. The seeds are used to randomise the turbulent field and sea states. The wind speed range is selected
 387 such as to avoid cut-in and cut-out events where the aerodynamic estimator is not expected to perform well. The turbulence

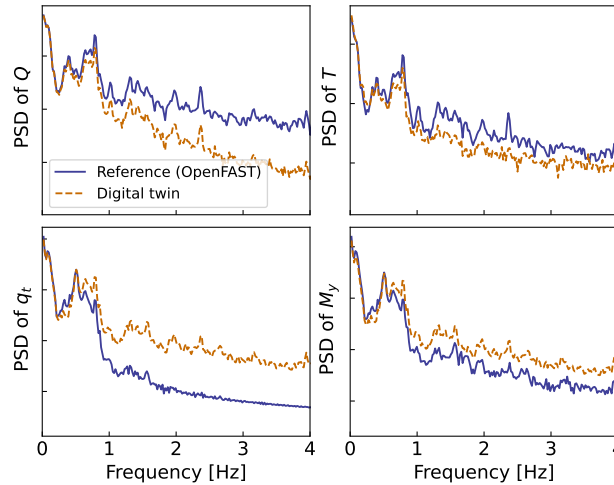


Figure 10. Power spectral density of the time series presented in Figure 9. A logarithmic scale is used on the y axis.

388 intensity is selected based on the normal turbulence model for a turbine of class “A”. The wave height and wave period are set
 389 as function of the wind speed as: $H_s(U) = 0.16U + 1$ and $T_p = 0.09U + 5.57$, based on the sea state measurements at the test
 390 site. OpenFAST simulations were run for each case, and then the digital twin was run using these numerical measurements. A
 summary of the mean relative error on some key estimated quantities is given in Figure 11. We observe that the mean relative

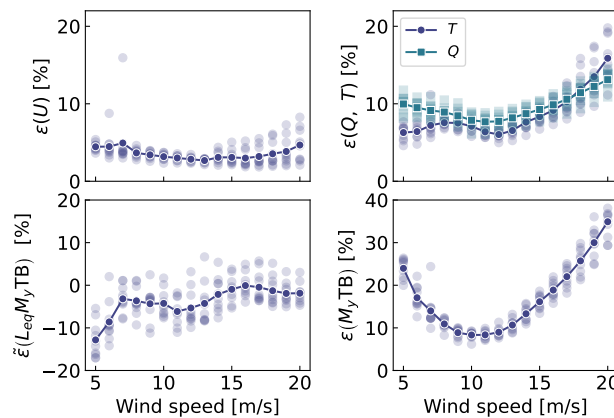


Figure 11. Mean relative error of estimated signals for various wind speed and seeds. Clockwise: wind speed (U), aerodynamic loads, tower-bottom moment (M_y TB), and damage equivalent load of the tower-bottom moment (L_{eq, M_y} TB). The individual simulations are indicated by transparent markers. The average over each seed is indicated using plain lines.

391
 392 error of the wind speed and aerodynamic loads are between 5% and 15% with a tendency for larger errors on the aerodynamic
 393 loads at low and high wind speeds. The error further propagates within the system and the tower-bottom moment is estimated
 394 with a relative error between 10% and 40%. The error levels indicate that the aerodynamic estimator, which is based on quasi-



395 steady rotor-averaged aerodynamics, cannot fully capture the dynamic aerodynamic state of the rotor in floating conditions.
396 In general, the digital twin lacks sufficient information to fully capture the tower-top loads and the frequency content of the
397 system. It is expected that placing additional sensors, such as accelerometers or load cells along the tower, can significantly
398 improve the estimation of the tower loads (in that case, we would either use OpenFAST linearization outputs, or, an extended
399 Kalman filter and a non-linear model for the outputs). As seen in Figure 11, the relative error levels on the damage equivalent
400 loads are between -10% and 5% , with the loads being either overestimated or underestimated depending on the wind speed.
401 The structural health monitoring system could potentially use the estimated error levels indicated in Figure 11 to provide a
402 confidence interval on the fatigue life time of the tower. We note that these error levels represent a best case scenario, because
403 we assumed that no noise or biases were present in the measurements. We expect the error levels to increase with additional
404 measurement noise.

405 4.2 Estimations using measurements from the full-scale prototype

406 In this section, we use measurements from the full-scale TetraSpar prototype installed off the Norwegian coast. Four days
407 of data were selected based on data availability; a wide range of wind speeds are present in the time series. Two days were
408 selected in summer and two in winter to account for potential seasonality. Apart from these criteria, the selection of time
409 series can be considered random. The measurement data is stored as 10-min time series sampled at 25 Hz. The total number
410 of 10-min samples used over the four days is 576. The measurement data is provided to the digital twin to perform the state
411 estimation and virtual sensing. The state estimation is currently 10 times faster than realtime. The virtual sensing step is half
412 realtime but computational improvements are possible, in particular, by using a compiled language instead of Python. The
413 prototype is equipped with load cells at the tower top, middle and bottom, and nacelle wind speed measurements. We use these
414 measurements to compare with the digital twin estimates. A sample of results is provided in Figure 12. The figure illustrates
415 a selected case where the estimation of the tower load is reasonably accurate, with an error on the damage equivalent load of
only 0.4% . We note that the wind speed from the measurement is a point measurement, and it is therefore not expected to be

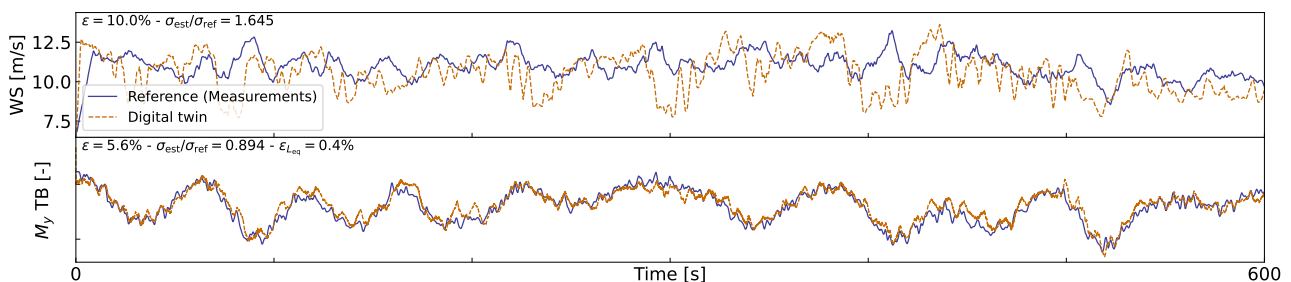


Figure 12. Comparison of digital twin outputs with wind speed and tower-bottom moment measurements from the TetraSpar prototype. The measured wind speed comes from a nacelle anemometer and therefore is expected to differ from the rotor-averaged value estimated by the digital twin.

416

417 in strong agreement with the digital twin estimate which is representative of a rotor-averaged wind speed.



An aggregate of results from all the 10-min digital twin runs is illustrated in Figure 13. The figure shows relative errors in

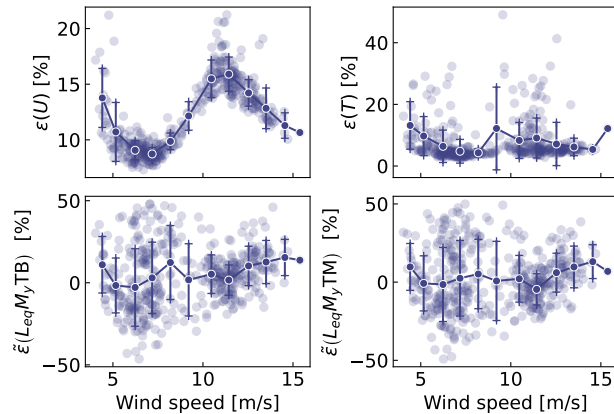


Figure 13. Similar to Figure 11 but using measurements from the Tetra Spar prototype. Each marker indicate a 10 min simulation result. The bottom plots are for the tower bottom (TB) and tower middle (TM) bending moments.

418

419 wind speed, thrust, and damage equivalent loads at the tower bottom and tower middle. As indicated previously, the wind speed
 420 from the digital twin and the measurements are different quantities, but the level of error obtained indicates that the digital twin
 421 is able to capture the main level of wind speed. The aerodynamic thrust from the aerodynamic estimator is compared with the
 422 load cell at the tower top in the fore-aft direction. This is a **crude first-order approximation**, but the overall estimated levels
 423 appears to be on average around 10% from the measured ones. The tower damage equivalent loads are on average within $\pm 10\%$
 424 of the values obtained from the measurements, but some cases show errors ranging between $\pm 50\%$. To give perspective on
 the large values taken by the metrics, we illustrate two cases with large errors in Figure 14 and Figure 15. In both cases, we

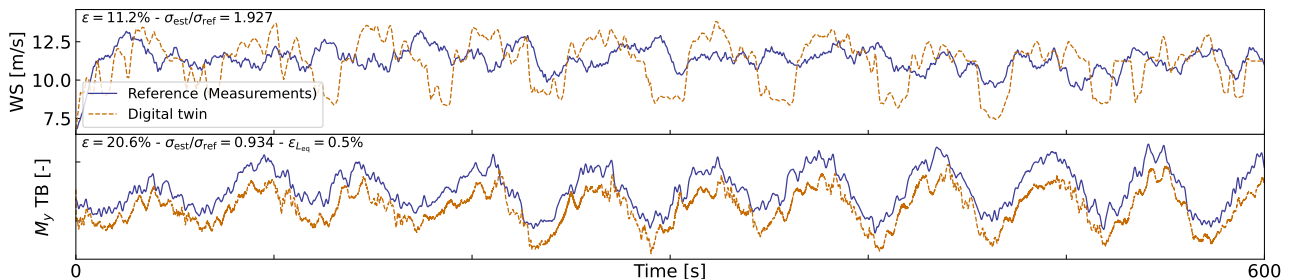


Figure 14. Similar to Figure 12, but for a case where a clear offset is present in the tower loads.

425

426 observe that the estimator is capturing the trends and low frequencies with accuracies that, from a pure qualitative perspective,
 427 would appear satisfactory. As seen in Figure 14, an offset is present in the signal, which indicates that some physics might be
 428 missing from the load virtual sensing, or that the state estimator is failing. In Figure 14, the overall load level is well captured,
 429 but the error in the damage equivalent load is $\epsilon_{L_{eq}}$ is 33%. As illustrated in Figure 10, our current method fails at capturing the

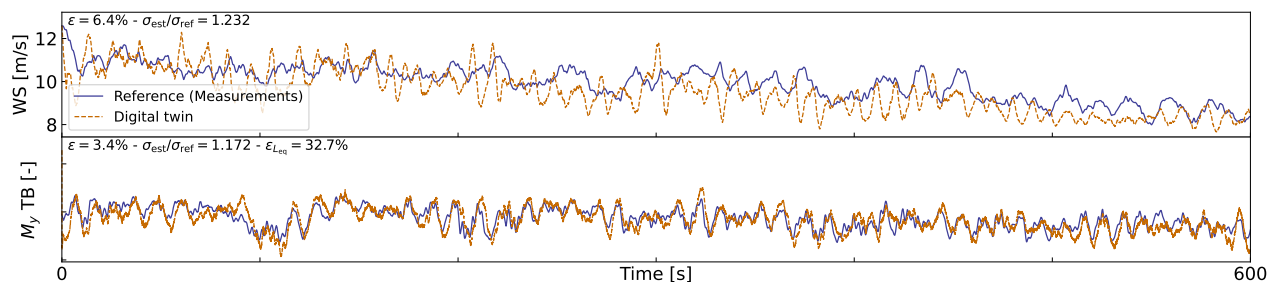


Figure 15. Similar to Figure 12, but for a case where a large error in damage equivalent load is observed.

430 high-frequency content of the signals, which can have a significant impact on the accuracy of the damage equivalent loads. In
431 spite of these challenges, the average accuracy of 10% is promising and indicates that the current methodology can be used to
432 reconstruct some structural and environmental signals from a limited number of readily-available sensors.

433 5 Conclusions

434 In this work, we implemented, verified, and validated a physics-based digital twin solution applied to a floating offshore wind
435 turbine. The work focused on the estimation of the aerodynamic loads and the section loads along the tower, using a set of
436 measurements that we expect to be available on any existing wind turbine (power, pitch, rotor speed, and tower acceleration),
437 and motion sensors that are likely to be standard measurements for a floating platform (inclination and GPS sensors). The key
438 concept behind our approach consists in using: 1) a Kalman filter to estimate the structural states based on a linear model of the
439 structure and measurements from the turbine, 2) an aerodynamic estimator, and 3) a physics-based virtual sensing procedure
440 to obtain the loads along the tower. An important part of the work consisted in developing the methodology and implementing
441 the tools and models necessary for the aerodynamic estimation, state estimation, and load virtual sensing. We explored two
442 different pathways to obtain models: a suite of Python tools, or OpenFAST linearization. We used components from both
443 approaches for the digital twin.

444 Using numerical experiments, we found that the accuracy of the individual models were typically in the order of 5%. When
445 comparing the digital twin estimations with the measurements from the TetraSpar prototype, the errors increased to 10%-
446 15% on average for the quantities of interest. Overall, the accuracy of the results appeared promising given the scope of our
447 work, which aimed at illustrating a proof of concept for a floating wind turbine digital twin. We observed non-negligible
448 scatter of results for the estimation of the tower damage equivalent loads that we attributed to the difficulty of capturing
449 high-frequency content. Future work, should therefore explore possible improvements of the method to address this issue.
450 Additional improvements could include: gain-scheduling of the linear models, using nonlinear models and extended Kalman
451 filtering techniques, introducing additional degrees of freedom and a full account of the yawing of the nacelle, adding a model
452 to account for wave excitation forces, introducing additional measurements, improving the robustness of the aerodynamic



453 estimator (in particular beyond the cut-in and cut-out wind speed), and expanding the virtual sensing steps to estimate additional
454 signals.

455 *Author contributions.* EB implemented the digital twin and wrote the main corpus of this paper. JJ, CB and JZ provided continuous feedback
456 on the project and reviewed the article.

457 *Competing interests.* No competing interests are present.

458 *Code availability.* The revised version of this paper will contain a Zenodo link for the repository <https://github.com/NREL/wtdigitwin>. The
459 source code of the digital twin and examples using a generic spar turbine are provided in the github repository.

460 *Acknowledgements.* This work was authored in part by the National Renewable Energy Laboratory, operated by Alliance for Sustainable
461 Energy, LLC, for the U.S. Department of Energy (DOE) under Contract No. DE-AC36-08GO28308. Funding provided by U.S. Department
462 of Energy Office of Energy Efficiency and Renewable Energy Wind Energy Technologies Office. The views expressed in the article do
463 not necessarily represent the views of the DOE or the U.S. Government. The U.S. Government retains and the publisher, by accepting the
464 article for publication, acknowledges that the U.S. Government retains a nonexclusive, paid-up, irrevocable, worldwide license to publish or
465 reproduce the published form of this work, or allow others to do so, for U.S. Government purposes.

466 *Financial support.* This work was funded under the Technology Commercialization Fund Project, supported by the DOE's Wind Energy
467 Technologies Office.

468 **Appendix A: Linearization of the equations of motion with augmented inputs**

469 In this section, we describe the procedure used to linearize the structural equations of motion without a knowledge of the external loads,
470 which is used to obtain Equation 1. We write the implicit form of the equations of motion as

$$471 \mathbf{e}(\mathbf{q}, \dot{\mathbf{q}}, \ddot{\mathbf{q}}, \tilde{\mathbf{u}}, t) = \mathbf{0} \tag{A1}$$

472 where \mathbf{q} , $\dot{\mathbf{q}}$, $\ddot{\mathbf{q}}$ and $\tilde{\mathbf{u}}$ are the degrees of freedom, velocities, accelerations and “augmented inputs” of the model, respectively. The term
473 augmented input is used because the external loads are included in this vector. The external loads are (in general) a function of the degrees
474 of freedom. Therefore, we write the augmented input vector as:

$$475 \tilde{\mathbf{u}} = \tilde{\mathbf{u}}(\mathbf{q}, \dot{\mathbf{q}}, \ddot{\mathbf{q}}, \mathbf{u}) \tag{A2}$$



476 where \mathbf{u} is the vector of inputs in the classical sense, that is, consisting of system inputs that do not depend on the degrees of freedom (for
 477 instance, the wave elevation). The operating point is written using the subscript “0”, and defined as:

$$478 \quad \mathbf{e}(\mathbf{q}_0, \dot{\mathbf{q}}_0, \ddot{\mathbf{q}}_0, \tilde{\mathbf{u}}_0, t) = \mathbf{0} \quad (\text{A3})$$

479 We perturb each variable, as $\mathbf{q} = \mathbf{q}_0 + \delta\mathbf{q}$, $\dot{\mathbf{q}} = \dot{\mathbf{q}}_0 + \delta\dot{\mathbf{q}}$, etc., where δ indicates a small perturbation of the quantities. The perturbation of the
 480 augmented input is then:

$$481 \quad \tilde{\mathbf{u}} = \tilde{\mathbf{u}}(\mathbf{q}_0, \dot{\mathbf{q}}_0, \ddot{\mathbf{q}}_0, \mathbf{u}_0) + \left. \frac{\partial \tilde{\mathbf{u}}}{\partial \mathbf{q}} \right|_0 \delta\mathbf{q} + \left. \frac{\partial \tilde{\mathbf{u}}}{\partial \dot{\mathbf{q}}} \right|_0 \delta\dot{\mathbf{q}} + \left. \frac{\partial \tilde{\mathbf{u}}}{\partial \ddot{\mathbf{q}}} \right|_0 \delta\ddot{\mathbf{q}} + \left. \frac{\partial \tilde{\mathbf{u}}}{\partial \mathbf{u}} \right|_0 \delta\mathbf{u} \quad (\text{A4})$$

482 where $|_0$ indicates that the expressions are evaluated at the operating point. The linearized equations are obtained using a Taylor-Series
 483 expansion:

$$484 \quad \left[M_0 - Q_0 \left. \frac{\partial \tilde{\mathbf{u}}}{\partial \ddot{\mathbf{q}}} \right|_0 \right] \delta\ddot{\mathbf{q}} + \left[C_0 - Q_0 \left. \frac{\partial \tilde{\mathbf{u}}}{\partial \dot{\mathbf{q}}} \right|_0 \right] \delta\dot{\mathbf{q}} + \left[K_0 - Q_0 \left. \frac{\partial \tilde{\mathbf{u}}}{\partial \mathbf{q}} \right|_0 \right] \delta\mathbf{q} = Q_0 \left. \frac{\partial \tilde{\mathbf{u}}}{\partial \mathbf{u}} \right|_0 \delta\mathbf{u} \quad (\text{A5})$$

485 with

$$486 \quad M_0 = - \left. \frac{\partial \mathbf{e}}{\partial \ddot{\mathbf{q}}} \right|_0, \quad C_0 = - \left. \frac{\partial \mathbf{e}}{\partial \dot{\mathbf{q}}} \right|_0, \quad K_0 = - \left. \frac{\partial \mathbf{e}}{\partial \mathbf{q}} \right|_0, \quad Q_0 = \left. \frac{\partial \mathbf{e}}{\partial \mathbf{u}} \right|_0 \quad (\text{A6})$$

487 and where M_0 , C_0 , K_0 are the linear mass, damping, and stiffness matrices, Q_0 is the linear forcing vector, also called input matrix.

488 Appendix B: Transfer of a Jacobian from one destination point to another

489 The Jacobians provided by OpenFAST and MAP are provided at given nodes of the structure (e.g. the hydrodynamic nodes, or the fairleads).
 490 In this section, we highlight the procedure to transfer these Jacobians to another node (the platform reference point) assuming a rigid-body
 491 relationship between the nodes. The procedure is used in this work to compute the linear 6×6 matrix for the hydrodynamics and mooring
 492 dynamics in Section 3.3.2. We obtain different relationships depending if the destination point is assumed to be displaced or not.

493 B1 Transfer of Jacobians between two points

We consider a point source (noted S) and a destination point (noted D). The notations are illustrated in Figure B1. We assume a rigid-body

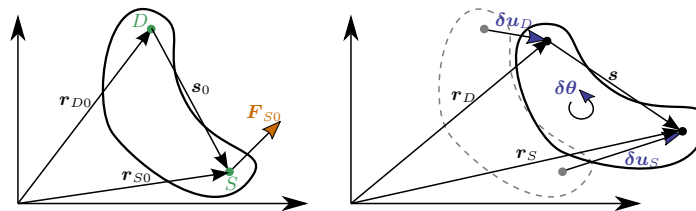


Figure B1. Rigid-body kinematics with the loads from one source point (S) transferred to a destination point (D), assuming small motion of the points.

494

495 relationship between the two points. The forces and moments at the destination and source are related as follows:

$$496 \quad \mathbf{F}_D = \mathbf{F}_S \quad (\text{B1})$$

$$497 \quad \mathbf{M}_D = \mathbf{M}_S + \tilde{\mathbf{s}}\mathbf{F}_S \quad (\text{B2})$$



498 where $\mathbf{s} = \mathbf{r}_S - \mathbf{r}_D$ is the vector from destination point to the source point, \mathbf{F}_S and \mathbf{M}_S are the force and moments, respectively, at point
 499 S , and the tilde notation refers to the skew symmetric matrix which is a matrix representation of the cross product. We seek to linearize
 500 Equation B1 and Equation B2 for small displacements and rotations of the destination and source nodes. In particular, we seek to express
 501 the Jacobians at the destination node as function of the source node, assuming a rigid-body relationship between the two. The rigid-body
 502 relationship linking the small displacements ($\delta\mathbf{u}$) and small rotations ($\delta\boldsymbol{\theta}$) of the source and destination points is:

$$503 \quad \delta\mathbf{u}_D = \delta\mathbf{u}_S + \tilde{\mathbf{s}}_0\delta\boldsymbol{\theta}_S$$

$$504 \quad \delta\boldsymbol{\theta}_D = \delta\boldsymbol{\theta}_S \tag{B3}$$

505 where \mathbf{s}_0 is the vector between the source and destination points at the operating point (prior to the perturbation). The Jacobians of the
 506 transformations given in Equation B3 (and its inverse) are:

$$507 \quad \begin{bmatrix} \frac{\partial\mathbf{u}_D}{\partial\mathbf{u}_S} & \frac{\partial\mathbf{u}_D}{\partial\boldsymbol{\theta}_S} \\ \frac{\partial\boldsymbol{\theta}_D}{\partial\mathbf{u}_S} & \frac{\partial\boldsymbol{\theta}_D}{\partial\boldsymbol{\theta}_S} \end{bmatrix} = \begin{bmatrix} \mathbf{I} & \tilde{\mathbf{s}}_0 \\ \mathbf{0} & \mathbf{I} \end{bmatrix}, \quad \begin{bmatrix} \frac{\partial\mathbf{u}_S}{\partial\mathbf{u}_D} & \frac{\partial\mathbf{u}_S}{\partial\boldsymbol{\theta}_D} \\ \frac{\partial\boldsymbol{\theta}_S}{\partial\mathbf{u}_D} & \frac{\partial\boldsymbol{\theta}_S}{\partial\boldsymbol{\theta}_D} \end{bmatrix} = \begin{bmatrix} \mathbf{I} & -\tilde{\mathbf{s}}_0 \\ \mathbf{0} & \mathbf{I} \end{bmatrix} \tag{B4}$$

508 To linearize Equation B1 and Equation B2, we introduce the following perturbations:

$$509 \quad \mathbf{F}_D = \mathbf{F}_{D0} + \delta\mathbf{F}_D, \quad \mathbf{F}_S = \mathbf{F}_{S0} + \delta\mathbf{F}_S \tag{B5}$$

$$510 \quad \mathbf{M}_D = \mathbf{M}_{D0} + \delta\mathbf{M}_D, \quad \mathbf{M}_S = \mathbf{M}_{S0} + \delta\mathbf{M}_S, \tag{B6}$$

511 where the subscript 0 indicates values at the operating point. At the operating point, Equation B1 and Equation B2 are satisfied, that is:

$$512 \quad \mathbf{F}_{D0} = \mathbf{F}_{S0} \tag{B7}$$

$$513 \quad \mathbf{M}_{D0} = \mathbf{M}_{S0} + \tilde{\mathbf{s}}_0\mathbf{F}_{S0} \tag{B8}$$

514 **Transfer of forces**

515 Inserting Equation B5 into Equation B1 leads to:

$$516 \quad \mathbf{F}_{D0} + \delta\mathbf{F}_D = \mathbf{F}_{S0} + \delta\mathbf{F}_S \tag{B9}$$

517 Which, using Equation B7, leads to:

$$518 \quad \delta\mathbf{F}_D = \delta\mathbf{F}_S \tag{B10}$$

519 The Jacobians of the loads at node D with respect to the displacements at node D are then obtained by applying the chain rule to Equation B10
 520 and making use of the Jacobian of the displacements given in the right of Equation B4. For instance, for the force:

$$521 \quad \frac{\partial\mathbf{F}_D}{\partial\mathbf{u}_D} = \frac{\partial\mathbf{F}_S}{\partial\mathbf{u}_S} \frac{\partial\mathbf{u}_S}{\partial\mathbf{u}_D} + \frac{\partial\mathbf{F}_S}{\partial\boldsymbol{\theta}_S} \frac{\partial\boldsymbol{\theta}_S}{\partial\mathbf{u}_D} = \frac{\partial\mathbf{F}_S}{\partial\mathbf{u}_S}$$

$$522 \quad \frac{\partial\mathbf{F}_D}{\partial\boldsymbol{\theta}_D} = \frac{\partial\mathbf{F}_S}{\partial\mathbf{u}_S} \frac{\partial\mathbf{u}_S}{\partial\boldsymbol{\theta}_D} + \frac{\partial\mathbf{F}_S}{\partial\boldsymbol{\theta}_S} \frac{\partial\boldsymbol{\theta}_S}{\partial\boldsymbol{\theta}_D} = \frac{\partial\mathbf{F}_S}{\partial\boldsymbol{\theta}_S} - \frac{\partial\mathbf{F}_S}{\partial\mathbf{u}_S} \tilde{\mathbf{s}}_0 \tag{B11}$$

523 For the transfer of the moments, the relationship will be different whether the moments are transferred at the undisplaced destination point,
 524 or the displaced destination point.



525 Moments at the undisplaced destination point

526 In this section, the moments are transferred to the undisplaced destination point. The vector from undisplaced destination point to the
 527 displaced source is:

$$528 \quad \mathbf{r} = \mathbf{s}_0 + \delta \mathbf{u}_S \quad (\text{B12})$$

529 Introducing Equation B6 and Equation B12 into Equation B2, and temporarily using the “×” notation instead of the tilde notation:

$$530 \quad \mathbf{M}_{D0} + \delta \mathbf{M}_D = \mathbf{M}_{S0} + \delta \mathbf{M}_S + \mathbf{s}_0 \times \mathbf{F}_{S0} + \mathbf{s}_0 \times \delta \mathbf{F}_S + \delta \mathbf{u}_S \times \mathbf{F}_{S0} + \delta \mathbf{u}_S \times \delta \mathbf{F}_S \quad (\text{B13})$$

531 Making use of Equation B8, neglecting the non-linear term ($\delta \mathbf{u}_S \times \delta \mathbf{F}_S$) and reintroducing the tilde notation, leads to:

$$532 \quad \delta \mathbf{M}_D = \delta \mathbf{M}_S + \tilde{\mathbf{s}}_0 \delta \mathbf{F}_S - \tilde{\mathbf{F}}_{S0} \delta \mathbf{u}_S \quad (\text{B14})$$

533 The Jacobians of the moments at the undisplaced node D with respect to the displacements at node D are then obtained by applying the
 534 chain rule to Equation B14:

$$535 \quad \frac{\partial \mathbf{M}_D}{\partial \mathbf{u}_D} = \frac{\partial \mathbf{M}_S}{\partial \mathbf{u}_S} \frac{\partial \mathbf{u}_S}{\partial \mathbf{u}_D} + \frac{\partial \mathbf{M}_S}{\partial \boldsymbol{\theta}_S} \frac{\partial \boldsymbol{\theta}_S}{\partial \mathbf{u}_D} + \tilde{\mathbf{s}}_0 \left[\frac{\partial \mathbf{F}_S}{\partial \mathbf{u}_S} \frac{\partial \mathbf{u}_S}{\partial \mathbf{u}_D} + \frac{\partial \mathbf{F}_S}{\partial \boldsymbol{\theta}_S} \frac{\partial \boldsymbol{\theta}_S}{\partial \mathbf{u}_D} \right] - \tilde{\mathbf{F}}_{S0} \frac{\partial \mathbf{u}_S}{\partial \mathbf{u}_D}$$

$$536 \quad = \frac{\partial \mathbf{M}_S}{\partial \mathbf{u}_S} + \tilde{\mathbf{s}}_0 \frac{\partial \mathbf{F}_S}{\partial \mathbf{u}_S} - \tilde{\mathbf{F}}_{S0} \quad (\text{B15})$$

537 and

$$538 \quad \frac{\partial \mathbf{M}_D}{\partial \boldsymbol{\theta}_D} = \frac{\partial \mathbf{M}_S}{\partial \boldsymbol{\theta}_S} \frac{\partial \boldsymbol{\theta}_S}{\partial \boldsymbol{\theta}_D} + \frac{\partial \mathbf{M}_S}{\partial \mathbf{u}_S} \frac{\partial \mathbf{u}_S}{\partial \boldsymbol{\theta}_D} + \tilde{\mathbf{s}}_0 \left[\frac{\partial \mathbf{F}_S}{\partial \boldsymbol{\theta}_S} \frac{\partial \boldsymbol{\theta}_S}{\partial \boldsymbol{\theta}_D} + \frac{\partial \mathbf{F}_S}{\partial \mathbf{u}_S} \frac{\partial \mathbf{u}_S}{\partial \boldsymbol{\theta}_D} \right] - \tilde{\mathbf{F}}_{S0} \frac{\partial \mathbf{u}_S}{\partial \boldsymbol{\theta}_D}$$

$$539 \quad = \frac{\partial \mathbf{M}_S}{\partial \boldsymbol{\theta}_S} - \frac{\partial \mathbf{M}_S}{\partial \mathbf{u}_S} \tilde{\mathbf{s}}_0 + \tilde{\mathbf{s}}_0 \frac{\partial \mathbf{F}_S}{\partial \boldsymbol{\theta}_S} - \tilde{\mathbf{s}}_0 \frac{\partial \mathbf{F}_S}{\partial \mathbf{u}_S} \tilde{\mathbf{s}}_0 + \tilde{\mathbf{F}}_{S0} \tilde{\mathbf{s}}_0 \quad (\text{B16})$$

540 Jacobian relationships at the undisplaced destination point

541 Equation B11, Equation B16 and Equation B15 can be gathered in matricial form to relate the different Jacobians between the source point
 542 and the undisplaced destination point:

$$543 \quad \begin{bmatrix} \frac{\partial \mathbf{F}_D}{\partial \mathbf{u}_D} & \frac{\partial \mathbf{F}_D}{\partial \boldsymbol{\theta}_D} \\ \frac{\partial \mathbf{M}_D}{\partial \mathbf{u}_D} & \frac{\partial \mathbf{M}_D}{\partial \boldsymbol{\theta}_D} \end{bmatrix}_{\text{undisplaced}} = \begin{bmatrix} \mathbf{I} & \mathbf{0} \\ \tilde{\mathbf{s}}_0 & \mathbf{I} \end{bmatrix} \begin{bmatrix} \frac{\partial \mathbf{F}_S}{\partial \mathbf{u}_S} & \frac{\partial \mathbf{F}_S}{\partial \boldsymbol{\theta}_S} \\ \frac{\partial \mathbf{M}_S}{\partial \mathbf{u}_S} & \frac{\partial \mathbf{M}_S}{\partial \boldsymbol{\theta}_S} \end{bmatrix} \begin{bmatrix} \mathbf{I} & -\tilde{\mathbf{s}}_0 \\ \mathbf{0} & \mathbf{I} \end{bmatrix} + \begin{bmatrix} \mathbf{0} & \mathbf{0} \\ -\tilde{\mathbf{F}}_{S0} & \tilde{\mathbf{F}}_{S0} \tilde{\mathbf{s}}_0 \end{bmatrix} \quad (\text{B17})$$

544 Moments at the displaced destination point

545 In this section, the moments are transferred to the displaced destination point. The vector from the displaced destination point to the displaced
 546 source is:

$$547 \quad \mathbf{r} = \mathbf{s}_0 + \delta \mathbf{u}_S - \delta \mathbf{u}_D = \mathbf{s}_0 - \tilde{\mathbf{s}}_0 \delta \boldsymbol{\theta}_S \quad (\text{B18})$$

548 Introducing Equation B6 and Equation B18 into Equation B2, and temporarily using the “×” notation instead of the tilde notation:

$$549 \quad \mathbf{M}_{D0} + \delta \mathbf{M}_D = \mathbf{M}_{S0} + \delta \mathbf{M}_S + \mathbf{s}_0 \times \mathbf{F}_{S0} + \mathbf{s}_0 \times \delta \mathbf{F}_S - (\mathbf{s}_0 \times \delta \boldsymbol{\theta}_S) \times \mathbf{F}_{S0} - (\mathbf{s}_0 \times \delta \boldsymbol{\theta}_S) \times \delta \mathbf{F}_S \quad (\text{B19})$$



550 Making use of Equation B8, neglecting the non-linear term $((s_0 \times \delta\theta_S) \times \delta F_S)$ and reintroducing the tilde notation, leads to:

$$551 \quad \delta M_D = \delta M_S + \tilde{s}_0 \delta F_S + \tilde{F}_{S0} \tilde{s}_0 \delta \theta_S \quad (\text{B20})$$

552 The Jacobians of the loads at the displaced node D with respect to the displacements at node D are then obtained by applying the chain rule
 553 to Equation B20 and making use of the Jacobian of the displacements given in the right of Equation B4.

$$554 \quad \frac{\partial M_D}{\partial u_D} = \frac{\partial M_S}{\partial u_S} \frac{\partial u_S}{\partial u_D} + \frac{\partial M_S}{\partial \theta_S} \frac{\partial \theta_S}{\partial u_D} + \tilde{s}_0 \frac{\partial F_S}{\partial u_S}$$

$$555 \quad = \frac{\partial M_S}{\partial u_S} + \tilde{s}_0 \frac{\partial F_S}{\partial u_S} \quad (\text{B21})$$

556 and

$$557 \quad \frac{\partial M_D}{\partial \theta_D} = \frac{\partial M_S}{\partial u_S} \frac{\partial u_S}{\partial \theta_D} + \frac{\partial M_S}{\partial \theta_S} \frac{\partial \theta_S}{\partial \theta_D} + \tilde{s}_0 \frac{\partial F_S}{\partial \theta_D} + \tilde{F}_{S0} \tilde{s}_0$$

$$558 \quad = \frac{\partial M_S}{\partial \theta_S} - \frac{\partial M_S}{\partial u_S} \tilde{s}_0 + \tilde{s}_0 \frac{\partial F_S}{\partial \theta_D} + \tilde{F}_{S0} \tilde{s}_0$$

$$559 \quad = \frac{\partial M_S}{\partial \theta_S} - \frac{\partial M_S}{\partial u_S} \tilde{s}_0 + \tilde{s}_0 \frac{\partial F_S}{\partial \theta_S} - \tilde{s}_0 \frac{\partial F_S}{\partial u_S} \tilde{s}_0 + \tilde{F}_{S0} \tilde{s}_0 \quad (\text{B22})$$

560 Jacobian relationships at the displaced destination point

561 Equation B11, Equation B22 and Equation B21 can be gathered in matricial form to relate the different Jacobians:

$$562 \quad \begin{bmatrix} \frac{\partial F_D}{\partial u_D} & \frac{\partial F_D}{\partial \theta_D} \\ \frac{\partial M_D}{\partial u_D} & \frac{\partial M_D}{\partial \theta_D} \end{bmatrix}_{\text{displaced}} = \begin{bmatrix} I & 0 \\ \tilde{s}_0 & I \end{bmatrix} \begin{bmatrix} \frac{\partial F_S}{\partial u_S} & \frac{\partial F_S}{\partial \theta_S} \\ \frac{\partial M_S}{\partial u_S} & \frac{\partial M_S}{\partial \theta_S} \end{bmatrix} \begin{bmatrix} I & -\tilde{s}_0 \\ 0 & I \end{bmatrix} + \begin{bmatrix} 0 & 0 \\ 0 & \tilde{F}_{S0} \tilde{s}_0 \end{bmatrix} \quad (\text{B23})$$

563 B2 Relationships at the displaced destination point for multiple source points

564 We now consider the case where multiple point sources are present. The derivation can be seen as a generalization of the previous case between two points, **but special care is needed**. The notations are illustrated in Figure B2. The loads at the destination points are obtained as:

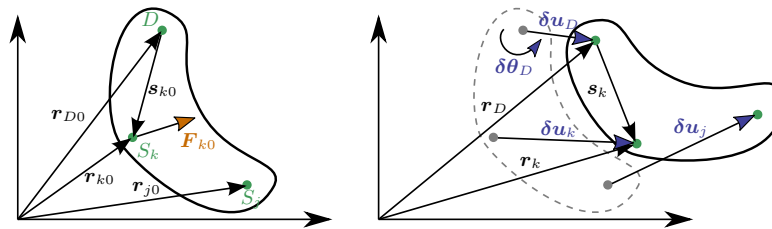


Figure B2. Rigid-body kinematics with the loads from multiple source points (S_j), transferred to a destination point (D)

565

$$566 \quad F_D = \sum_k F_k \quad (\text{B24})$$

$$567 \quad M_D = \sum_k M_k + \tilde{s}_k F_k \quad (\text{B25})$$



568 where k is an index looping over all points of the rigid structure. To shorten notations, we define the vector between the destination point and
 569 a given point as:

$$570 \quad \mathbf{s}_k = \mathbf{r}_k - \mathbf{r}_D \quad (\text{B26})$$

$$571 \quad \mathbf{s}_{k0} = \mathbf{r}_{k0} - \mathbf{r}_{D0} \quad (\text{B27})$$

572 where \mathbf{s}_k is the vector between the displaced points and \mathbf{s}_{k0} is the vector prior to the displacement (at the operating condition). Due to the
 573 rigid-body assumption, the elementary displacements of the points are related as follows:

$$574 \quad \delta \mathbf{u}_D = \delta \mathbf{u}_j + \tilde{\mathbf{s}}_{j0} \delta \boldsymbol{\theta}_j$$

$$575 \quad \delta \boldsymbol{\theta}_D = \delta \boldsymbol{\theta}_j \quad (\text{B28})$$

576 from which one obtains the following useful relationships:

$$577 \quad \frac{\partial \mathbf{u}_j}{\partial \mathbf{u}_D} = \mathbf{I}, \quad \frac{\partial \boldsymbol{\theta}_j}{\partial \mathbf{u}_D} = \mathbf{O}, \quad \frac{\partial \mathbf{u}_j}{\partial \boldsymbol{\theta}_D} = -\tilde{\mathbf{s}}_{j0}, \quad \frac{\partial \boldsymbol{\theta}_j}{\partial \boldsymbol{\theta}_D} = \mathbf{I}, \quad \frac{\partial \boldsymbol{\theta}_j}{\partial \boldsymbol{\theta}_k} = \mathbf{I} \delta_{jk}, \quad \frac{\partial \boldsymbol{\theta}_j}{\partial \mathbf{u}_k} = \mathbf{O} \quad (\text{B29})$$

578 Using a similar Taylor expansion as for the case with two nodes, the perturbation loads are obtained as:

$$579 \quad \delta \mathbf{F}_D = \sum_k \delta \mathbf{F}_k \quad (\text{B30})$$

$$580 \quad \delta \mathbf{M}_D = \sum_k \delta \mathbf{M}_k + \tilde{\mathbf{s}}_{k0} \delta \mathbf{F}_k + \tilde{\mathbf{F}}_{k0} (\tilde{\mathbf{s}}_{k0} \delta \boldsymbol{\theta}_k) \quad (\text{B31})$$

581 The chain rule for a given quantity of interest (Q) is obtained by summing over all the elementary variables:

$$582 \quad dQ = \sum_j \frac{\partial Q}{\partial \mathbf{u}_j} d\mathbf{u}_j + \frac{\partial Q}{\partial \boldsymbol{\theta}_j} d\boldsymbol{\theta}_j \quad (\text{B32})$$

583 For instance, the application of the chain rule to \mathbf{F}_D and using Equation B30 leads to:

$$584 \quad \frac{\partial \mathbf{F}_D}{\partial \mathbf{u}_D} = \sum_j \frac{\partial \mathbf{F}_D}{\partial \mathbf{u}_j} \frac{\partial \mathbf{u}_j}{\partial \mathbf{u}_D} + \frac{\partial \mathbf{F}_D}{\partial \boldsymbol{\theta}_j} \frac{\partial \boldsymbol{\theta}_j}{\partial \mathbf{u}_D} = \sum_j \sum_k \frac{\partial \mathbf{F}_k}{\partial \mathbf{u}_j} \frac{\partial \mathbf{u}_j}{\partial \mathbf{u}_D} + \frac{\partial \mathbf{F}_k}{\partial \boldsymbol{\theta}_j} \frac{\partial \boldsymbol{\theta}_j}{\partial \mathbf{u}_D} = \sum_j \sum_k \frac{\partial \mathbf{F}_k}{\partial \mathbf{u}_j} \quad (\text{B33})$$

585 Eventually, the Jacobians at the displaced destination node are obtained as:

$$586 \quad \left[\begin{array}{cc} \frac{\partial \mathbf{F}_D}{\partial \mathbf{u}_D} & \frac{\partial \mathbf{F}_D}{\partial \boldsymbol{\theta}_D} \\ \frac{\partial \mathbf{M}_D}{\partial \mathbf{u}_D} & \frac{\partial \mathbf{M}_D}{\partial \boldsymbol{\theta}_D} \end{array} \right]_{\text{displaced}} = \sum_j \left\{ \sum_k \left(\left[\begin{array}{cc} \mathbf{I} & \mathbf{0} \\ \tilde{\mathbf{s}}_{k0} & \mathbf{I} \end{array} \right] \left[\begin{array}{cc} \frac{\partial \mathbf{F}_k}{\partial \mathbf{u}_j} & \frac{\partial \mathbf{F}_k}{\partial \boldsymbol{\theta}_j} \\ \frac{\partial \mathbf{M}_k}{\partial \mathbf{u}_j} & \frac{\partial \mathbf{M}_k}{\partial \boldsymbol{\theta}_j} \end{array} \right] \left[\begin{array}{cc} \mathbf{I} & -\tilde{\mathbf{s}}_{j0} \\ \mathbf{0} & \mathbf{I} \end{array} \right] \right) + \left[\begin{array}{cc} \mathbf{0} & \mathbf{0} \\ \mathbf{0} & \tilde{\mathbf{F}}_{j0} \tilde{\mathbf{s}}_{j0} \end{array} \right] \right\} \quad (\text{B34})$$

587 Appendix C: Verification of the linear models

588 In this section, we supplement the results given in Section 3.3.3, by showing free-decay results without hydrodynamics (no added mass,
 589 damping, hydrostatics). We show results with the structure only in Figure C1, and results with the structure and moorings in Figure C2.
 590 These results also include the nonlinear WELIB formulation. A strong agreement is found between the nonlinear OpenFAST and WELIB
 591 models, and between the linear OpenFAST and WELIB models. The yaw degree of freedom appears to be more challenging to capture for
 592 the linear models.

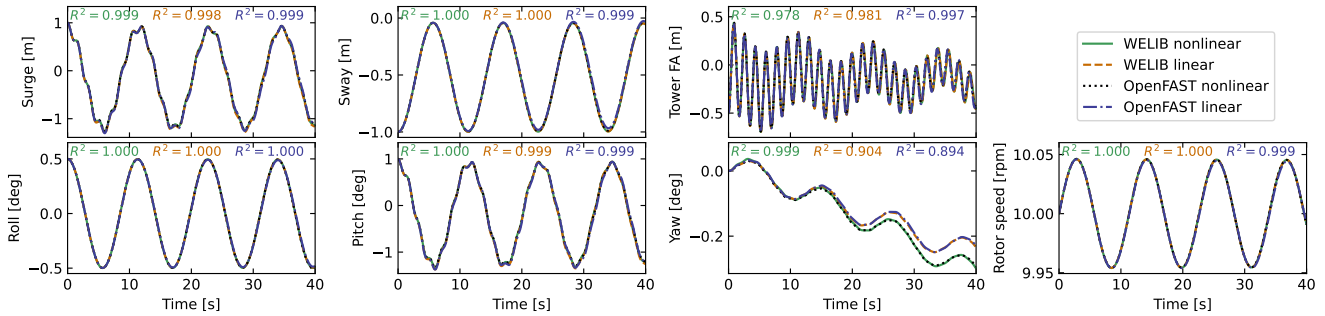


Figure C1. Free decay of the structure using non linear and linear models for a case including only the structure (no moorings, no hydrodynamics). Time series of the main DOFs.

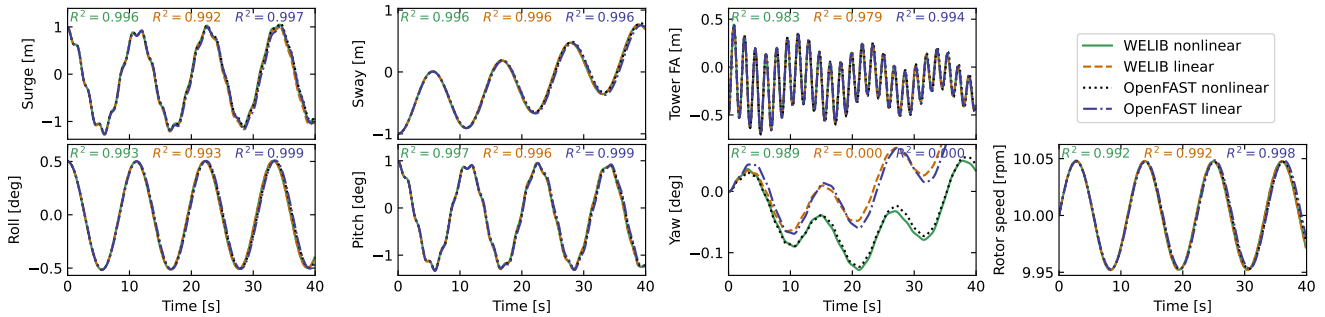


Figure C2. Free decay of the structure using non linear and linear models for a case including moorings (no hydrodynamics). Time series of the main DOFs.

593 Appendix D: Computation of section loads

594 In this section, we describe the nonlinear calculation procedure used in Section 3.6.2 to assess the section loads along the tower based on
 595 estimates of the structure kinematics and the loads at the tower top. For conciseness, in this appendix, we use x and z for the coordinates
 596 along the tower fore-aft and tower height, respectively, instead of x_T and z_T .

597 D1 Tower fore-aft bending moment and shear force

598 The fore-aft and side-side loads are computed the same way, therefore this section focuses on the fore-aft direction. The sectional fore-aft
 599 bending moment at a given tower height z is determined as:

$$600 \mathcal{M}_y(z) = \mathcal{M}_{y,\text{top}} - \int_z^{L_T} S_x(z') dz' \quad (\text{D1})$$

601 where $\mathcal{M}_{y,\text{top}}$ is the fore-aft bending moment at the tower top and S_x is the shear force in the x direction, obtained as:

$$602 S_x(z) = \int_z^{L_T} p_{x,\text{all}}(z') dz' \quad (\text{D2})$$



603 where $p_{x,\text{all}}$ is the force per length acting on the tower section in the fore-aft direction, including contributions from the external loads
 604 (aerodynamic loads on the structure), inertial loads due to the acceleration of the structure (including gravity), and nonlinear correction terms
 605 from the loads in the z direction ($p - \Delta$ effect, including self-weight effects). The different contributions are written as follows:

$$606 \quad p_{x,\text{all}} = p_{x,\text{ext}} + p_{x,\text{corr}} - p_{x,\text{acc}} \quad (\text{D3})$$

607 In this work, we neglect the external loads on the tower, $p_{x,\text{ext}} = 0$ (aerodynamic loads on the tower are typically small relative to rotor-thrust
 608 loads for an operating wind turbine). The acceleration contribution is $p_{x,\text{acc}} = -m(z)(a_{x,\text{struct}}(z) - a_{x,\text{grav}})$, where m is the mass per length
 609 along the beam, and $a_{x,\text{struct}}(z)$ is the acceleration of the section, determined based on the rigid-body acceleration of the floater and the elastic
 610 motion of the tower (\dot{q}_T and \ddot{q}_T), and $a_{x,\text{grav}}$ is the acceleration of gravity in the x direction. The $p - \Delta$ correction term due to the vertical
 611 loading is computed as (see Branlard (2019)):

$$612 \quad p_{x,\text{corr}} = \frac{d^2\Phi}{dz^2} \left[\int_z^L p_z dx' + \sum_{z_k \geq z} \mathcal{F}_{z,k} \right] - \frac{d\Phi}{dz} \left[p_z + \sum_k \mathcal{F}_{z,k} \delta(z - z_k) \right] \quad (\text{D4})$$

613 where p_z is the vertical load per length (mostly consisting of the self-weight), $\mathcal{F}_{z,k}$ is the k -th vertical force acting at point z_k , and δ is the
 614 Dirac function, and Φ is the shape function used to describe the tower displacement field (see Section 2.3.3). In our case, only the vertical
 615 force acting on top of the tower is present, $z_1 = L_T$ and $\mathcal{F}_{z,1} = \mathcal{F}_{z,\text{top}}$. The procedure is similar to compute the section loads in the y direction
 616 (using the $p - \Delta$ correction as well).

617 D2 Tower and RNA kinematics

618 The determination of the tower section loads require a knowledge of the tower kinematics, to compute $\mathbf{a}_{\text{struct}}$, and the RNA kinematics, to
 619 compute the inertial contribution to the tower top loads (see Section D3). The position, linear velocity, linear acceleration, rotational speed,
 620 and rotational acceleration of the floater (point F , body f) are given respectively by:

$$621 \quad \mathbf{r}_F = \{x, y, z\}_i, \quad \mathbf{v}_F = \{\dot{x}, \dot{y}, \dot{z}\}_i, \quad \mathbf{a}_F = \{\ddot{x}, \ddot{y}, \ddot{z}\}_i, \quad (\text{D5})$$

$$622 \quad \boldsymbol{\omega}_f = \{\dot{\phi}_z, \dot{\phi}_y, \dot{\phi}_x\}_i, \quad \dot{\boldsymbol{\omega}}_f = \{\ddot{\phi}_z, \ddot{\phi}_y, \ddot{\phi}_x\}_i \quad (\text{D6})$$

623 where the notation i indicates that the coordinates of the vector are expressed in the inertial coordinate system. The transformation matrix
 624 from the floater to the inertial frame is obtained as: $\mathbf{R}_{f2i} = \mathbf{R}(\phi_x, \phi_y, \phi_z)$; where \mathbf{R} is a function computing the rotation matrix. The tower
 625 base (point T , body t) kinematics are obtained from the floater using rigid body kinematics:

$$626 \quad \mathbf{r}_T = \mathbf{r}_F + \mathbf{r}_{FT}, \quad (\text{D7})$$

$$627 \quad \mathbf{v}_T = \mathbf{v}_F + \boldsymbol{\omega}_f \times \mathbf{r}_{FT}, \quad (\text{D8})$$

$$628 \quad \mathbf{a}_T = \mathbf{a}_F + \boldsymbol{\omega}_f \times (\boldsymbol{\omega}_f \times \mathbf{r}_{FT}) + \dot{\boldsymbol{\omega}}_f \times \mathbf{r}_{FT}, \quad (\text{D9})$$

$$629 \quad \boldsymbol{\omega}_t = \boldsymbol{\omega}_f, \quad \dot{\boldsymbol{\omega}}_t = \dot{\boldsymbol{\omega}}_f, \quad \mathbf{R}_{t2i} = \mathbf{R}_{f2i} \quad (\text{D10})$$



630 where \mathbf{r}_{FT} is the vector from the floater point to the tower base. The kinematics of a given tower section (point S , at height z) are given by:

$$631 \quad \mathbf{r}_S = \mathbf{r}_T + \mathbf{r}_{TS} = \mathbf{r}_T + \mathbf{r}_{TS_0} + \mathbf{u}_S, \quad (\text{D11})$$

$$632 \quad \mathbf{v}_S = \mathbf{v}_T + \boldsymbol{\omega}_t \times \mathbf{r}_{TS} + \dot{\mathbf{u}}_S, \quad (\text{D12})$$

$$633 \quad \mathbf{a}_S = \mathbf{a}_T + \boldsymbol{\omega}_t \times (\boldsymbol{\omega}_t \times \mathbf{r}_{TS}) + \dot{\boldsymbol{\omega}}_t \times \mathbf{r}_{TS} + 2\boldsymbol{\omega}_t \times \dot{\mathbf{u}}_S + \ddot{\mathbf{u}}_S, \quad (\text{D13})$$

$$634 \quad \boldsymbol{\omega}_s = \boldsymbol{\omega}_t + \boldsymbol{\omega}_{ts}, \quad (\text{D14})$$

$$635 \quad \dot{\boldsymbol{\omega}}_s = \dot{\boldsymbol{\omega}}_t + \dot{\boldsymbol{\omega}}_{ts} + \boldsymbol{\omega}_t \times \boldsymbol{\omega}_{ts}, \quad (\text{D15})$$

636 where $\mathbf{r}_{TS_0} = z\hat{\mathbf{z}}_t$ is the vector from the tower base to the undeflected section, \mathbf{u}_S , $\dot{\mathbf{u}}_S$, $\ddot{\mathbf{u}}_S$ are the elastic motions of the section computed
 637 based on the shape function and the generalized coordinates, e.g. $\mathbf{u}_S(z) = \sum_j q_{t,j} \boldsymbol{\Phi}_j = q_t \boldsymbol{\Phi}(z) \hat{\mathbf{x}}_t$ (see e.g. Branlard and Geisler (2022)).
 638 We note that OpenFAST also includes a vertical motion (~~referred to as a “geometric nonlinearity”~~) associated with the deflection, which we
 639 are currently neglecting in this work. The transformation matrix from the section to the tower is $\mathbf{R}_{s2t} = \mathbf{R}(-u'_{S,y}, u'_{S,x}, 0)$, where $u_{S,y}$ and
 640 $u_{S,x}$ are the components of \mathbf{u}_S in the tower coordinate system, and the prime notation indicates the differentiation with respect to z . The
 641 rotation speed and acceleration of the tower section with respect to the tower base are:

$$642 \quad \boldsymbol{\omega}_{ts} = \{\dot{u}'_{S,y}, \dot{u}'_{S,x}, 0\}_t, \quad \dot{\boldsymbol{\omega}}_{ts} = \{\ddot{u}'_{S,y}, \ddot{u}'_{S,x}, 0\}_t \quad (\text{D16})$$

643 The kinematics of the tower-top point and nacelle (point N , body n) are taken from the last section node (point S with $z = L_T$). Yawing,
 644 tilting, and rolling of the tower top would change the orientation matrix, rotational velocity and rotational acceleration of the nacelle. These
 645 kinematics are omitted here for conciseness. The kinematics of the center of mass of the RNA (point G) are obtained using rigid-body
 646 kinematics (identical to what was used between point F and T).

647 D3 Tower-top loads

648 The tower-top loads are computed as follows:

$$649 \quad \mathcal{F}_{\text{top}} = \mathcal{F}_{\text{aero}} - \mathcal{F}_{\text{inertia}} \quad (\text{D17})$$

$$650 \quad \mathcal{M}_{\text{top}} = \mathcal{M}_{\text{aero}} - \mathcal{M}_{\text{inertia}} \quad (\text{D18})$$

651 where the aerodynamic loads are transferred to the tower top and where the inertial loads from the rigid-body RNA are:

$$652 \quad \mathcal{F}_{\text{inertia}} = M_{\text{RNA}}(\mathbf{a}_G - \mathbf{g}) \quad (\text{D19})$$

$$653 \quad \mathcal{M}_{\text{inertia}} = \mathbf{r}_{NG} \times \mathcal{F}_{\text{inertia}} + \mathbf{J}_G \cdot \dot{\boldsymbol{\omega}}_n + \boldsymbol{\omega}_n \times (\mathbf{J}_G \cdot \boldsymbol{\omega}_n) \quad (\text{D20})$$

654 where: \mathbf{r}_{NG} is the vector from the tower top to the center of mass of the RNA, M_{RNA} is the mass of the RNA, \mathbf{J}_G is the inertia tensor of the
 655 RNA at its center of mass, \mathbf{a}_G is the linear acceleration of the center of mass of the RNA, $\boldsymbol{\omega}_n$ is the rotational acceleration of the RNA, $\dot{\boldsymbol{\omega}}_n$
 656 is the rotational acceleration of the nacelle. The load calculation is first done in the coordinate system of the nacelle, and then transferred to
 657 the coordinate system of the tower where Equation D1 is defined.



658 References

- 659 Auger, F., Hilairet, M., Guerrero, J. M., Monmasson, E., Orlowska-Kowalska, T., and Katsura, S.: Industrial Applications of the Kalman
660 Filter: A Review, *IEEE Transactions on Industrial Electronics*, 60, 5458–5471, <https://doi.org/10.1109/TIE.2012.2236994>, 2013.
- 661 Bilbao, J., Lourens, E.-M., Schulze, A., and Ziegler, L.: Virtual sensing in an onshore wind turbine tower using a Gaussian process latent
662 force model, *Data-Centric Engineering*, 3, <https://doi.org/10.1017/dce.2022.38>, 2022.
- 663 Bossanyi, E. A.: Individual Blade Pitch Control for Load Reduction, *Wind Energy*, 6, 119–128, <https://doi.org/10.1002/we.76>, 2003.
- 664 Bottasso, C. and Croce, A.: Cascading Kalman Observers of Structural Flexible and Wind States for Wind Turbine Control, Tech. rep.,
665 Dipartimento di Ingegneria Aerospaziale, Politecnico di Milano, Milano, Italy, Scientific Report DIA-SR 09-02, 2009.
- 666 Boukhezzar, B. and Siguerdidjane, H.: Nonlinear Control of a Variable-Speed Wind Turbine Using a Two-Mass Model, *IEEE Transactions*
667 *on Energy Conversion*, 26, 149–162, <https://doi.org/10.1109/TEC.2010.2090155>, 2011.
- 668 Branlard, E.: Flexible multibody dynamics using joint coordinates and the Rayleigh-Ritz approximation: The general framework behind and
669 beyond Flex, *Wind Energy*, 22, 877–893, <https://doi.org/10.1002/we.2327>, 2019.
- 670 Branlard, E.: WELIB, Wind Energy Library, GitHub repository <http://github.com/eBranlard/welib/>, <https://doi.org/10.5281/zenodo.7306075>
671 Last accessed November 2022, 2022.
- 672 Branlard, E. and Geisler, J.: A symbolic framework for flexible multibody systems applied to horizontal-axis wind turbines, *Wind Energy*
673 *Science*, 2022.
- 674 Branlard, E., Giardina, D., and Brown, C. S. D.: Augmented Kalman filter with a reduced mechanical model to estimate tower loads on
675 a land-based wind turbine: a step towards digital-twin simulations, *Wind Energy Science*, 5, 1155–1167, [https://doi.org/10.5194/wes-5-](https://doi.org/10.5194/wes-5-1155-2020)
676 [1155-2020](https://doi.org/10.5194/wes-5-1155-2020), 2020a.
- 677 Branlard, E., Jonkman, J., Dana, S., and Doubrawa, P.: A digital twin based on OpenFAST linearizations for real-time load and fatigue esti-
678 mation of land-based turbines, *Journal of Physics: Conference Series*, 1618, 022 030, <https://doi.org/10.1088/1742-6596/1618/2/022030>,
679 2020b.
- 680 Castella, X. T.: Operations and maintenance costs for offshore wind farm analysis and strategies to reduce O&M costs, Master’s thesis,
681 Universitat Politècnica de Catalunya, and National Taiwan University of Science and Technology, 2020.
- 682 Cosack, N.: Fatigue Load Monitoring with Standard Wind Turbine Signals, Ph.D. thesis, Universität Stuttgart, 2010.
- 683 Dimitrov, N., Kelly, M. C., Vignaroli, A., and Berg, J.: From wind to loads: wind turbine site-specific load estimation with surrogate models
684 trained on high-fidelity load databases, *Wind Energy Science*, 3, 767–790, <https://doi.org/10.5194/wes-3-767-2018>, 2018.
- 685 Eftekhar Azam, S., Chatzi, E., and Papadimitriou, C.: A dual Kalman filter approach for state estimation via output-only acceleration mea-
686 surements, *Mechanical Systems and Signal Processing*, 60-61, 866 – 886, <https://doi.org/https://doi.org/10.1016/j.ymsp.2015.02.001>,
687 2015.
- 688 Evans, M., Han, T., and Shuchun, Z.: Development and validation of real time load estimator on Goldwind 6 MW wind turbine, *Journal of*
689 *Physics: Conference Series*, 1037, 032 021, <https://doi.org/10.1088/1742-6596/1037/3/032021>, 2018.
- 690 Iliopoulos, A., Shirzadeh, R., Weijtjens, W., Guillaume, P., Hemelrijck, D. V., and Devriendt, C.: A modal decomposition and expansion
691 approach for prediction of dynamic responses on a monopile offshore wind turbine using a limited number of vibration sensors, *Mechanical*
692 *Systems and Signal Processing*, 68-69, 84–104, <https://doi.org/https://doi.org/10.1016/j.ymsp.2015.07.016>, 2016.
- 693 Jacquelin, E., Bennani, A., and Hamelin, P.: Force reconstruction: analysis and regularization of a deconvolution problem, *Journal of Sound*
694 *and Vibration*, 265, 81 – 107, [https://doi.org/https://doi.org/10.1016/S0022-460X\(02\)01441-4](https://doi.org/https://doi.org/10.1016/S0022-460X(02)01441-4), 2003.



- 695 Jonkman, B. and Buhl, M.: TurbSim User's Guide, Tech. Rep. NREL/TP-500-39797, National Renewable Energy Laboratory, Golden,
696 Colorado, USA, <https://doi.org/10.2172/965520>, 2006.
- 697 Jonkman, B., Mudafort, R. M., Platt, A., Branlard, E., Sprague, M., Jonkman, J., Vijayakumar, G., Buhl, M., Ross, H., Bortolotti, P., Masciola,
698 M., Ananthan, S., Schmidt, M. J., Rood, J., Damiani, R., Mendoza, N., Hall, M., and Corniglion, R.: OpenFAST v3.4.1. Open-source wind
699 turbine simulation tool, available at <http://github.com/OpenFAST/OpenFAST/>, <https://doi.org/10.5281/zenodo.7632926>, 2023.
- 700 Jonkman, J. M. and Jonkman, B. J.: FAST modularization framework for wind turbine simulation: full-system linearization, *Journal of*
701 *Physics: Conference Series*, 753, 082 010, <https://doi.org/10.1088/1742-6596/753/8/082010>, 2016.
- 702 Jonkman, J. M., Wright, A. D., Hayman, G. J., and Robertson, A. N.: Full-System Linearization for Floating Offshore Wind Turbines in
703 OpenFAST, vol. ASME 2018 1st International Offshore Wind Technical Conference of *International Conference on Offshore Mechanics*
704 *and Arctic Engineering*, https://doi.org/10.1115/IOWTC2018-1025_v001T01A028, 2018.
- 705 Jonkman, J. M., Branlard, E., and Jasa, J. P.: Influence of wind turbine design parameters on linearized physics-based models in OpenFAST,
706 *Wind Energy Science*, 7, 559–571, <https://doi.org/10.5194/wes-7-559-2022>, 2022.
- 707 Kalman, R. E.: A new approach to linear filtering and prediction problems, *Journal of Basic Engineering*, 12, 35–45, 1960.
- 708 Kamel, O., Kretschmer, M., Pfeifer, S., Luhmann, B., Hauptmann, S., and Bottasso, C.: Data-driven virtual sensor for online loads estimation
709 of drivetrain of wind turbines, *Forschung im Ingenieurwesen*, pp. 1–8, <https://doi.org/10.1007/s10010-023-00615-4>, 2023.
- 710 Lourens, E., Reynders, E., Roeck, G. D., Degrande, G., and Lombaert, G.: An augmented Kalman filter for force identification in structural
711 dynamics, *Mechanical Systems and Signal Processing*, 27, 446–460, 2012.
- 712 Ma, C.-K. and Ho, C.-C.: An inverse method for the estimation of input forces acting on non-linear structural systems, *Journal of Sound and*
713 *Vibration*, 275, 953 – 971, [https://doi.org/https://doi.org/10.1016/S0022-460X\(03\)00797-1](https://doi.org/https://doi.org/10.1016/S0022-460X(03)00797-1), 2004.
- 714 Mehlan, F., R. Nejad, A., and Gao, Z.: Digital Twin Based Virtual Sensor for Online Fatigue Damage Monitoring in Offshore Wind Turbine
715 Drivetrains, *Journal of Offshore Mechanics and Arctic Engineering*, 144, 1–9, <https://doi.org/10.1115/1.4055551>, 2022.
- 716 Mehlan, F., Keller, J., and R. Nejad, A.: Virtual sensing of wind turbine hub loads and drivetrain fatigue damage, *Forschung im Ingenieur-*
717 *wesen*, pp. 1–12, <https://doi.org/10.1007/s10010-023-00627-0>, 2023.
- 718 Mendez Reyes, H., Kanev, S., Doekemeijer, B., and van Wingerden, J.-W.: Validation of a lookup-table approach to modeling turbine fatigue
719 loads in wind farms under active wake control, *Wind Energy Science*, 4, 549–561, <https://doi.org/10.5194/wes-4-549-2019>, 2019.
- 720 Noppe, N., Iliopoulos, A., Weijtjens, W., and Devriendt, C.: Full load estimation of an offshore wind turbine based on SCADA and ac-
721 celerometer data, *Journal of Physics: Conference Series*, 753, 072 025, <https://doi.org/10.1088/1742-6596/753/7/072025>, 2016.
- 722 Schröder, L., Dimitrov, N. K., Verelst, D. R., and Sørensen, J. A.: Wind turbine site-specific load estimation using artificial neural networks
723 calibrated by means of high-fidelity load simulations, *Journal of Physics: Conference Series*, 1037, 062 027, [https://doi.org/10.1088/1742-](https://doi.org/10.1088/1742-6596/1037/6/062027)
724 [6596/1037/6/062027](https://doi.org/10.1088/1742-6596/1037/6/062027), 2018.
- 725 Selvam, K., Kanev, S., van Wingerden, J. W., van Engelen, T., and Verhaegen, M.: Feedback–feedforward individual pitch control for wind
726 turbine load reduction, *International Journal of Robust and Nonlinear Control*, 19, 72–91, <https://doi.org/10.1002/rnc.1324>, 2009.
- 727 Song, Z., Hackl, C., Anand, A., Thommessen, A., Petzschmann, J., Kamel, O., Braunbehrens, R., Kaifel, A., Roos, C., and
728 Hauptmann, S.: Digital Twins for the Future Power System: An Overview and a Future Perspective, *Sustainability*, 15, 5259,
729 <https://doi.org/10.3390/su15065259>, 2023.
- 730 Stiesdal Offshore: The TetraSpar full scale demonstration project, [https://www.stiesdal.com/offshore-technologies/
731 the-tetraspar-full-scale-demonstration-project/](https://www.stiesdal.com/offshore-technologies/the-tetraspar-full-scale-demonstration-project/), 2022.



- 732 Zarchan, P. and Musoff, H.: Fundamentals of Kalman filtering : a practical approach, Fourth Edition, AIAA, Progress in astronautics and
733 aeronautics, 2015.
- 734 Ziegler, L., Smolka, U., Cosack, N., and Muskulus, M.: Brief communication: Structural monitoring for lifetime extension of offshore wind
735 monopiles: can strain measurements at one level tell us everything?, Wind Energy Science, 2, 469–476, [https://doi.org/10.5194/wes-2-](https://doi.org/10.5194/wes-2-469-2017)
736 469-2017, 2017.